Journal of Biomedical Materials Research Part A

WILEY

Society For Biomaterials

RESEARCH ARTICLE OPEN ACCESS

Electrically Conductive Injectable Silk/PEDOT: PSS Hydrogel for Enhanced Neural Network Formation

Rajiv Borah[1,2,3] | Julia O'Sullivan[4,5] | Meenakshi Suku[1,2] | Dahnan Spurling[3,6,7] | Daniel Diez Clarke[1,2] | Valeria Nicolosi[3,6,7] | Maeve A. Caldwell[4,5] | Michael G. Monaghan[1,2,3,8]

[1]Discipline of Mechanical, Manufacturing and Biomedical Engineering, Trinity College Dublin, Dublin 2, Ireland | [2]Trinity Centre for Biomedical Engineering, Trinity College Dublin, Dublin 2, Ireland | [3]Advanced Materials and Bio-Engineering Research (AMBER), Centre at Trinity College Dublin and the Royal College of Surgeons in Ireland, Dublin 2, Ireland | [4]Department of Physiology, School of Medicine, Trinity College Dublin, Dublin 2, Ireland | [5]Trinity College Institute of Neuroscience, Trinity College Dublin, Dublin 2, Ireland | [6]Centre for Research on Adaptive Nanostructures and Nanodevices (CRANN), Trinity College Dublin, Dublin 2, Ireland | [7]School of Chemistry, Trinity College Dublin, Dublin 2, Ireland | [8]CÚRAM, Research Ireland Centre for Research in Medical Devices, National University of Ireland, Galway, Ireland

Correspondence: Michael G. Monaghan (monaghmi@tcd.ie)

Received: 7 August 2024 | **Revised:** 6 December 2024 | **Accepted:** 12 December 2024

Funding: This work was supported by the European Union's Horizon 2020 Research and Innovation Programme under the Marie Skłodowska-Curie (Grant 101067283). M.G.M. and D.D.C. received funding from the CRY Ireland for Michael Greene Cardiac Risk in the Yong (CRY) Summer Scholarship (CRYUG/2023/001). The authors also acknowledge EPSRC and SFI Centre for Doctoral Training in Engineered Tissues for Discovery, Industry and Medicine, for funding this work (Grant EP/S02347X/1). V.N. and D.S. wish to thank the support of the EIC Transition Grant Super-HEART (Grant 101057679), the Research Ireland-funded AMBER Research Centre, and Frontiers for the Future Award (Grants 12/RC/2278_P2 and 20/FFP-A/8950, respectively).

Keywords: conductive hydrogel | human induced pluripotent stem cell (hiPSC) | injectable hydrogel | PEDOT:PSS | silk | spinal cord repair

ABSTRACT

With no effective treatments for functional recovery after injury, spinal cord injury (SCI) remains one of the unresolved healthcare challenges. Human induced pluripotent stem cell (hiPSC) transplantation is a versatile patient-specific regenerative approach for functional recovery after SCI. Injectable electroconductive hydrogel (ECH) can further enhance the cell transplantation efficacy through a minimally invasive manner as well as recapitulate the native bioelectrical microenvironment of neural tissue. Given these considerations, we report a novel ECH prepared through self-assembly facilitated in situ gelation of natural silk fibroin (SF) derived from mulberry *Bombyx mori* silk and electrically conductive PEDOT:PSS. PEDOT:PSS was pre-stabilized to prevent the potential delamination of its hydrophilic PSS chain under aqueous environment using 3% (v/v) (3-glycidyloxypropyl)trimethoxysilane (GoPS) and 3% (w/v) poly(ethylene glycol)diglycidyl ether (PeGDE). The resultant ECH formulations are easily injectable with standard hand force with flow point below 100 Pa and good shear-thinning properties. The ECH formulations with unmodified and GoPS-modified PEDOT:PSS, that is, SF/PEDOT and SF/PEDOT*GoP* maintain comparable elastic modulus to spinal cord (~10–60 kPa) under physiological condition, indicating their flexibility. The GoPS-modified ECHs also display improved structural recoverability (~70%–90%) as compared to the unmodified versions of the ECHs (~30%–80%), as indicated by the three interval time thixotropy (3ITT) test. Additionally, these ECHs possess electrical conductivity in the range of ~0.2–1.2 S/m comparable to spinal cord (1–10 S/m), indicating their ability to mimic native bioelectrical environment. Approximately 80% or more cell survival was observed when hiPSC-derived cortical neurons and astrocytes were encapsulated within these ECHs. These ECHs support the maturation of cortical neurons when embedded for 7 days, fostering the development of a complex, interconnected network of long axonal processes and promoting synaptogenesis. These results underline the potential of silk ECHs in cell transplantation therapy for spinal cord regeneration.

1 | Introduction

Spinal cord injury (SCI) has debilitating impacts in a patient's life due to severe disruption in the transfer of motor and sensory information between the brain and muscles. This disruption results in varying degrees of paralysis below the level of the injury, including loss of movement, sensation, bowel and bladder control, and sexual function, and includes depression in 11%–37% patients [1]. With no effective treatments for functional recovery after injury, SCI remains one of the unresolved healthcare challenges to date. SCI affected 6.4 million people in Europe with an incidence of 0.19 million during the period 1990–2016.

SCI, which is primarily caused by vehicle accidents, falls, and violence, affects the most active and productive age group (less then ~40 years old) of people. Current management options for SCI are costly, with a patient in the United States facing a lifetime expense of $2.4–$5 million, depending on the severity of the injury, and treatments still do not fully restore lost functions [1, 2]. Existing clinical interventions focus on leveraging the spared neurons/axonal pathways in treating the symptoms of the injury, which include early decompression surgery, mean arterial pressure, steroids (methylprednisolone sodium succinate (MPSS)), moderate hypothermia (33°C), motor training, and therapeutic electrical stimulation [3, 4]. Spinal cord has limited regenerative capacity due to its inability to produce growth factors and lack of physical support following cystic cavity formation after injury. SCI pathophysiology is further complicated by ischemia, neuroinflammation, scarring, excitotoxicity, ionic imbalance, and cell death [4]. Thus, no single regenerative or rehabilitative strategy has achieved full or near-full functional recovery after SCI.

Although intraspinal cell transplantation therapies have emerged as a promising and minimally invasive strategy to treat primary and secondary injury cascades in SCI, they have limitations in terms of efficacy and translation [5]. There is lack of consensus on the optimal transplanted cell type for recovery post-SCI. Stem cell-derived therapies may use immature progenitor cells, which may not differentiate into a desirable cell type [6]. Mature cell transplantation offers more control over final lineage commitment, but is more sensitive to procedures done before transplantation [7]. Recently, the advancement of human induced pluripotent stem cell (hiPSC) technology has been demonstrated to produce functional neuronal network or tissue resembling central nervous system with high efficiency, establishing it as an attractive cell type for SCI cell transplantation [8–14].

An optimum and efficient cell delivery technique is still needed as cell transplantation is traditionally plagued by low cell viability, with survival rates as low as 1% [6]. Traditional cell delivery using a syringe injection of cell suspension in aqueous buffer exposes the transplanted cells to shear forces, causing membrane damage, and cell death [15]. In this regard, injectable but thixotropic bioactive hydrogels can be utilized to encapsulate cells, allowing the majority of the hydrogel to go through the needle as a solid while adjacent edges to the needle wall flow as a fluid. As a result, it can limit shear stress exposure to a small fraction of cells, resulting in a better viable cell delivery yield [16]. Indeed, injectable viscous hydrogels, as opposed to preformed scaffolds, can fill and mold to the shape of a contusion SCI without requiring tissue removal and losing reparative activity and can act as a physical support to bridge the lesion and also integrate itself with the native tissue [4, 17]. Additionally, hydrogels can also be engineered for enhanced cell viability and neuronal regeneration, in particular, by mimicking the native tissue environment.

Given these considerations, we hypothesize that an injectable electroconductive hydrogel (ECH) formulation, designed to mimic the native bioelectrical environment of neural tissue and combined with hiPSC-derived cortical neurons, could offer a more advanced and patient-specific regenerative approach for addressing SCI. The ECH formulation offers the unique advantage of not only recapitulating the native bioelectrical microenvironment, but also promoting cell-to-cell communication and synaptic function [3, 4, 18]. Additionally, it provides a suitable platform for therapeutic localized electrical stimulation to enhance functional neuronal growth [3, 19]. Despite the significant potential and numerous advantages of injectable ECHs in soft bioelectronics, along with recent advancements in synthesis and characterization techniques as reviewed by Peñas-Núñez et al. [20], there have been few studies specifically focusing on the application of ECHs for spinal cord repair (SCR). However, recognizing their immense potential, research efforts employing ECHs for SCR have gradually increased in the last few years, with some studies demonstrating the benefits of electrical stimulation and combining it with ECHs for enhancing functional recovery after SCI [21–25]. Readers are also referred to elsewhere for a detailed overview on ECHs for SCR [26]. Notably, few studies have investigated the combination of ECHs with cell therapy for SCR [21, 27–30], a strategy that holds the potential for superior functional outcomes by harnessing the synergistic effects of both approaches. Further development and a deeper understanding of these synergistic impacts remain areas for ongoing research.

However, as mentioned earlier, fate-restricted, postmitotic matured neuronal cells with long axonal processes are highly mechanosensitive and cannot multiply and therefore, have limited efficacy in cell therapy applications. iPSC-derived neuronal cells have been previously demonstrated to generate functional neural networks with a good cell survival rate when encapsulated within bioactive but passive (nonconductive) hydrogels [8, 16, 31, 32]. Few conductive scaffolds were previously demonstrated to drive neurogenesis from iPSCs, while none showed any neural network formation [18, 33, 34]. In contrast, only one study reports hyaluronic acid based ECH incorporated with carbon nanotube and polypyrrole for enhanced neurogenesis of iPSC-derived neurons [35]. Therefore, appropriately designing the ECH formulation with the necessary bioactivity, mechanical properties, shear-thinning characteristics, and thixotropic behavior is crucial to ensure the survival of this specific cell type and facilitate the effective integration needed for functional neural network formation. Poly(3,4-ethylenedioxythiophene)–poly(styrene sulfonate) (PEDOT:PSS) is one of the widely investigated conductive polymer for neural interfacing and nerve repair, owing to its flexibility similar to plastics and excellent electronic conductivity

(~200 S/cm) similar to metals [36, 37]. PEDOT:PSS alone has been shown to form injectable hydrogels [38] and demonstrated good biocompatibility [39]. Interestingly, PEDOT:PSS has been demonstrated to exhibit mixed ionic and electronic conductivity in a hydrated environment and therefore, can match effectively with the ion transport in biological tissues [40, 41]. To enhance bioactivity and tissue adhesiveness, PEDOT:PSS has been combined with various bioactive molecules and biopolymers, such as polyethylene glycol–peptide [42], alginate [43], carboxymethyl cellulose–dopamine [44], gelatin or gelatin methacryloyl (GelMA) [45–48], heparin [49], and SF [50–52]. While most of these PEDOT:PSS based hydrogels were assessed with cell types other than neural cells, only few of the PEDOT-based hydrogels, which were combined with gelatin and GelMA were assessed with dorsal root ganglion [47] and primary rat neocortical astrocytes [48]. Recently, Gao et al. developed a 3D bioprinted scaffold composed of GelMA, hyaluronic acid, and PEDOT, loaded with rat neural stem cells (NSCs) [53]. Their study demonstrated that this conductive hydrogel formulation, combined with NSCs, enhanced neural regeneration, reduced glial scarring, and promoted improved myelination in a rat SCI transection model. Similar studies were also reported by Song et al. who developed PEDOT/gelatin/polyethylene glycol based rat NSC laden 3D bioprinted hydrogel scaffold for improved functional recovery after SCI with reduced glial scar formation [54, 55]. Though the investigation of PEDOT-based ECHs for SCR applications has begun recently; however, a minimally invasive approach has yet to be explored. PEDOT-based ECHs have been also largely underexplored with hiPSC-derived neural cells. A single study reported by Feig et al. encapsulated hiPSC-derived neural progenitor cells (NPCs) within PEDOT:PSS based injectable granular hydrogel and showed their viability till 5 days [56]. However, this study has not assessed the neural network formation ability or hiPSC-derived astrocyte viability within the hydrogel.

Therefore, in the present work, we utilize *Bombyx mori* SF, a high performance naturally derived protein with excellent biocompatibility, and tunable biodegradability to develop conductive hydrogels blended with PEDOT:PSS [57–59]. SF consists of unique amino acid sequences of large hydrophobic regions (AGSGAGA) separated by smaller hydrophilic regions, including some highly reactive amino acids like lysine, tyrosine, serine, aspartic acid, and glutamic acid [60, 61]. The unique hydrophobic–hydrophilic amino acid sequence makes it prone to self-assembly of its hydrophobic regions, resulting in in situ gelation in response to temperature changes, mechanical/shear forces, or even electric fields [57, 58]. Due to the reactive amino acids, SF can also be modified to tailor its physicochemical properties [60, 61]. The unique hydrophobic–hydrophilic amino acid sequence makes it prone to self-assembly of its hydrophobic regions, resulting in in situ gelation in response to temperature changes, mechanical/shear forces, or even electric fields [57, 58]. Taking this unique advantage, an injectable ECH has been prepared blending SF with PEDOT:PSS using a cross-linker free strategy. There have been concerns regarding the cytocompatibility of PEDOT:PSS, primarily due to its hydrophilic PSS chains, which can degrade or delaminate from PEDOT chains in an aqueous environment, leading to cytotoxic effects [37, 62, 63]. Hence, PEDOT:PSS was modified by 3% (v/v) hydrolyzed silane cross-linker, namely (3-glycidyloxypropyl)trimethoxysilane (GoPS) and poly(ethylene glycol)diglycidyl ether (PeGDE). Modifying PEDOT:PSS with PeGDE previously resulted in a highly hydrophilic scaffold with improved stability and conductivity [64]. While modification of GoPS was reported to reduce the conductivity of PEDOT:PSS, the resultant formulation demonstrated good biocompatibility [65]. Recently, GoPS-modified PEDOT:PSS was used to fabricate an ultra-comfortable nerve cuff for long-term interfacing with peripheral nerves, indicating the potential functional applications of GoPS-modified PEDOT:PSS in soft bioelectronics [66]. Nevertheless, the ECH formulations prepared with these unmodified and modified PEDOT:PSS variants were evaluated for their injectability and mechanical behavior, followed by cytocompatibility testing with C3H10 mouse embryonic fibroblasts. After optimizing the composition of the ECHs, they were further tested for mechanical stability, rotational rheometry, and electroconductivity including biodegradability and microstructural features. hiPSC-derived mature cortical neurons and astrocytes were encapsulated within the silk-based ECHs to confirm cell survival, and neuronal network formation was assessed after 7 days of culture using β(III) tubulin staining. The results demonstrate the potential of this approach for functional neural network formation in SCI treatment.

2 | Materials and Methods

2.1 | Materials

Degummed *Bombyx mori* silk fibers were received from Institute of Advanced Study in Science & Technology, Guwahati, India. Lithium bromide (LiBr) and high conductivity grade poly(3,4-ethylenedioxythiophene):poly(styrene sulfonate) (PEDOT:PSS) were purchased from Sigma-Aldrich. The majority of cell culture reagents including neurobasal medium, DMEM/F-12, fetal bovine serum (FBS), N-2 supplement, MEM nonessential amino acids (NEAA), β-mercaptoethanol, B-27 supplement, GlutaMAX, and penicillin–streptomycin (Pen-Strep) were acquired from Thermo Fisher Scientific. Dulbecco's Modified Eagle's Medium (DMEM) with low glucose for C3H10 cell culture was obtained from Sigma-Aldrich. The C3H10 T1/2 cell line was purchased from ATCC for initial evaluation of the materials' cytocompatibility. Calcein AM and ethidium monoazide bromide (EMA) were obtained from Cambridge Bioscience. Purified anti-tubulin β 3 (TUBB3) antibody (BL-801202) was obtained from BioLegend.

2.2 | Extraction of SF

Degummed silk fibers were digested in a 9.3 M LiBr solution at 60°C for 4 h. Typically, a 9.3 M LiBr solution was used to dissolve 5 g of degummed silk fibers, with a 1:4 ratio of silk to LiBr (i.e., 1 g of silk fibers in 4 mL of LiBr solution) [59]. The highly viscous SF solution was then dialyzed in distilled water for 48 h using a 12 kDa cellulose membrane (Sigma-Aldrich), with regular water changes every 8 h at room temperature. The dialyzed SF solution was then subjected to centrifugation at 5000 rpm for 10 min at 4°C to eliminate any undissolved particulates. The

concentration of the regenerated protein was calculated using the gravimetric method and then stored at a temperature of 4°C until it was ready to be used for subsequent experiments.

2.3 | Pre-Stabilization of PEDOT:PSS

To prevent the possible dissociation of PSS chains in aqueous environment [37, 63], commercially available 1.1 wt% PEDOT:PSS solution was modified with a hydrolyzed silane cross-linker, namely 3-GoPS and PeGDE (Figure 1A), following previous reports with slight modification [62]. Briefly, 3% (v/v) of GoPS was mixed with the PEDOT:PSS solution and subjected to 1 hour of sonication using a probe sonicator (VCX 130, Sonics & Materials Inc., USA) followed by heating at 100°C for another 1 h. Previous studies have modified PEDOT:PSS films or sponges using GoPS, with the cross-linking process requiring annealing at 140°C for 30–60 min [62, 65, 67, 68]. GoPS reacts with the negatively charged sulfonate groups ($-SO_3^-$) in the PSS chains of PEDOT:PSS through ring-opening reactions of its epoxy groups, which requires overcoming a certain activation energy barrier (Figure S1). Therefore, a heat treatment is a critical step to induce this covalent cross-linking [68, 69]. GoPS has a boiling point of 120°C, which means that PEDOT dispersions modified with GoPS exhibit a higher boiling point compared to pure water, consistent with previous reports [70, 71]. The beaker was covered during heating to prevent any evaporation. PEDOT:PSS solution was also modified using 3% (w/v) PeGDE to enhance its long-term stability. To obtain a uniform

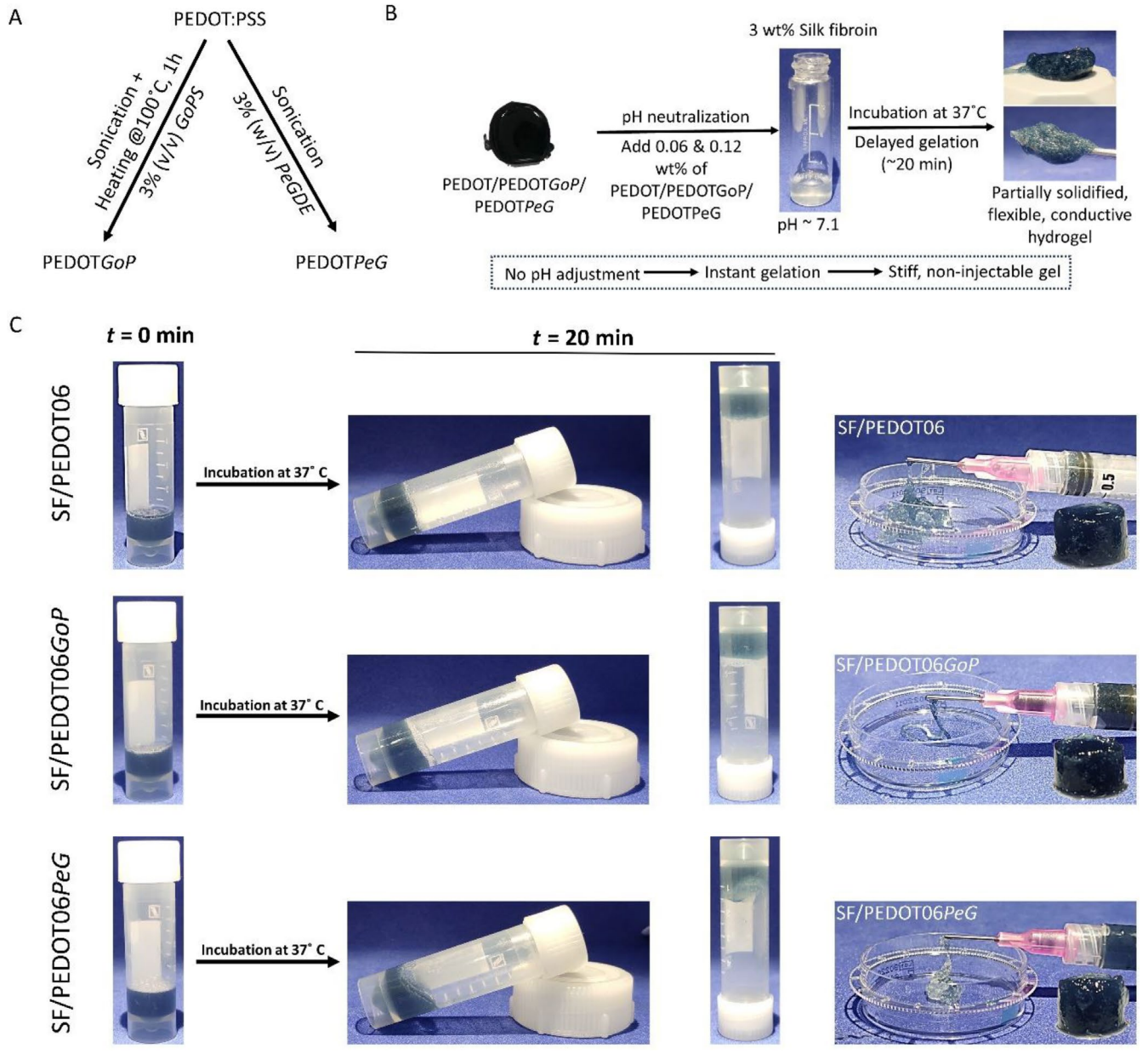

FIGURE 1 | (A) Schematic of PEDOT:PSS pre-stabilization using GoPS and PeGDE. (B) Representative preparation process of SF/PEDOT:PSS based conductive hydrogel highlighting the role pH adjustment step, which delayed the gelation process resulting in flexible injectable hydrogel, while without pH adjustment (at acidic pH) stiff, non-injectable hydrogel is formed. (C) Gelation of different variants of electroconductive hydrogels (ECHs) under incubation at 37°C for 20 min, showing inversion test results and their injectability with representative visual images.

mixture, PEDOT-PeGDE solution was also probe sonicated for 1 h. The GoPS and PeGDE modified PEDOT:PSS variants are denoted as PEDOT*GoP* and PEDOT*PeG*, respectively.

2.4 | Preparation of Injectable SF/PEDOT:PSS Based Conductive Hydrogel

The scheme of preparation of SF/PEDOT:PSS hydrogels is shown in Figure 1B. Briefly, the pH of unmodified and modified PEDOT:PSS variants were neutralized prior to mixing with SF solution. Commercially available PEDOT:PSS variants are acidic in nature (pH < 4), which interacts aggressively with SF solution, resulting in an inhomogeneous and phase-separated hydrogel formulation, which are not practically injectable (Figure S3). The increased protonation of lysine residues (i.e., $—NH_3^+$) in SF at low pH leads to strong Coulombic electrostatic interactions with the negatively charged sulfonate groups (i.e., $—SO_3^-$) in the PSS of PEDOT:PSS, causing rapid gelation [58, 72]. In contrast, at neutral pH, the partially deprotonated carboxyl groups (—COO^-) in SF show electrostatic repulsion with the negatively charged SO_3^- groups of PSS, which may contribute to the slower gelation process [58]. Hence, pH neutralized PEDOT:PSS variants were mixed with 2 or 3 wt% of SF solution and incubated at 37°C for 20–30 min hydrogel formation. Previously, 0.52% PEDOT:PSS was reported to be toxic to embedded cells within its hydrogels [73]. Therefore, two concentrations, namely 0.06 and 0.12 wt% of different PEDOT:PSS variants, that is, unmodified PEDOT:PSS, PEDOT*GoP*, and PEDOT*PeG* were used for fabricating the ECHs. The different ECHs codes are described in Table 1.

2.5 | Physicochemical Characterization

2.5.1 | Gelation Kinetics Study

Gelation kinetics were assessed in terms of change in ECH turbidity using UV–Visible absorption spectroscopic method as reported elsewhere [58]. 200 μL of different ECHs variants (Table 1) including pure SF solution were incubated in a covered 96 well plate at 37°C and absorbance at 550 nm was recorded at every 3 min up to 26 min and then, at 5 min interval up to 70 min using a multiplate-reader (Synergy HT Multi-Mode Microplate Reader, BioTek Instruments, USA) equipped with temperature control. Pure SF (3 wt%) was used as a control. The process of gelation of SF results in the formation of a varied microstructure, which in turn leads to an elevated level of light scattering within the visible range. This ultimately leads to an increase in turbidity, resulting in an increase in absorbance at 550 nm. The gelation time point (when the solution begins to gel) was identified as the time point when the average absorbance reached half of its maximum value, while the gelation process was considered complete when the absorbance stabilized at a saturated level [58, 74].

2.5.2 | FT-IR Spectroscopy

The secondary structure of the various ECHs was investigated using FT-IR Spectrum 100 with ATR (Perkin Elmer). Transmission and absorption spectra of freeze-dried ECH scaffolds were recorded within a spectral range of 4000–650 cm^{-1} at a 1 cm^{-1} interval and 16 scans. To determine different components of SF secondary structure, amide I regions (1705–1590 cm^{-1}) of the absorption spectra of all the samples were analyzed following a protocol reported elsewhere [57, 58]. Briefly, second derivative spectra was extracted from sample absorption spectrum by using a third degree polynomial function with a 9-point Savitski–Golay smoothing function, which was then subjected to Gaussian peak deconvolution method using OriginPro 2024 software [57, 58]. Briefly, second derivative spectra was extracted from sample absorption spectrum by using a third degree polynomial function with a 9-point Savitski–Golay smoothing function, which was then subjected to Gaussian peak deconvolution method using OriginPro 2024 software. The average percent composition of fibroin secondary structures including β sheet structure (indicator for silk gelation) was calculated by integrating the area of each deconvoluted curve and then normalizing to the total area of the amide I region. The peaks in the range of 1695–1700, 1666–1685, 1650–1660, 1635–1645, 1610–1635, 1600–1610 cm^{-1} are attributed to different SF secondary structures such as antiparallel β sheet, loops or turns, α helices, random coils, parallel β sheet, and side chains, respectively [57, 58, 75].

2.5.3 | Compression Test

The mechanical properties of different ECHs were evaluated in terms of their uniaxial unconfined compressive strength using a Zwick Universal testing machine mounted with a Zwick 200 N load cell (Zwick Roell, UK). Hydrogel samples, 1 h post-gelation, were cut into cylindrical shape with a dimension of 5 × 5 mm and compression was conducted with a preload of 0.1 N and at a compression rate of 0.1 mm s^{-1} up to 80% compression strain

TABLE 1 | Sample codes with their composition.

	PEDOT:PSS variants	Concentration (wt%)	Sample code of ECHs
Silk fibroin (SF)	PEDOT:PSS	0.06	SF/PEDOT06
		0.12	SF/PEDOT12
	PEDOT*GoP*	0.06	SF/PEDOT06*GoP*
		0.12	SF/PEDOT06*GoP*
	PEDOT*PeG*	0.06	SF/PEDOT06*PeG*
		0.12	SF/PEDOT12*PeG*

at room temperature. The compressive modulus was calculated as the slope of the linear elastic region of the stress–strain curve. For confirming the mechanical stability in aqueous environments, ECHs were incubated in 1× phosphate buffer solution (PBS, pH = 7.4) for 24 h prior to the compression test. All measurements were carried out for $n = 3$ samples per group.

2.5.4 | Rheological Assessment

All silk-based hydrogel formulations were evaluated for viscosity, dynamic viscoelastic behavior, and structural recovery under shear stress through rotational shear rheometry using an Anton Paar MCR102e rheometer. The hydrogel samples were assessed 1 h post-gelation with dimension of 8 mm diameter and 5 mm height at a physiological temperature (37°C). Viscosity tests were performed across a shear rate range of 0.1–250 s^{-1} encompassing 21 datapoints. For amplitude measurements, shear strain from 0.01% to 100% was applied over different silk-based hydrogels at an angular frequency of 10 $rads^{-1}$. The change in storage (G') and loss (G'') modulus was displayed against changing shear stress to find out the flow point (crossover of G' and G''). The three interval time thixotropy (3ITT) test was conducted to assess the hydrogel's ability to recover its structural integrity. The 3ITT test measures viscosity during three consecutive shearing intervals as a function of time to determine how much of the initial viscosity can be recovered and the time required for recovery. Ideally, an injectable or printable material should flow instantly under stress and regain its viscoelastic properties once the stress is removed. In this test, the first interval measures the viscosity of the viscoelastic fluid at low shear, followed by a high shear interval to simulate structural breakdown under conditions such as those experienced at the walls of a printing nozzle. Finally, the viscosity is measured again at a low shear interval to monitor structural recovery. For injectable or printable materials, a good recovery parameter is considered to be at least 80% of the original structural properties, ensuring sufficient layer stacking ability while maintaining the material's initial mechanical characteristics [76]. In this test, the hydrogel samples were first subjected to a low shear strain of 1% at 1 Hz for 120 s (1st interval), followed by a high shear strain of 500% at 1 Hz for 120 s (2nd interval), and finally the stress was released with a shear strain of 1% at the same frequency for 240 s (3rd interval).

2.5.5 | Conductivity Test

Electrical conductivity of different ECHs was tested using a source meter (Keithley 2400, Tektronix, USA) in customized two probe set up. Hydrogel samples were positioned between two parallel brass plates and current–voltage (I–V) characteristics were recorded under potential sweep from −1 to +1 V range at an increment of 40 mV s^{-1}. The measurement was conducted with the hydrogel samples with an approximate dimension of 5 × 5 mm (diameter and height).

The conductivity (σ) of various samples was determined using the following formula:

$$\sigma = \frac{L}{RA}$$

Here, R and A are the resistance and area of the sample, whereas L is the distance between the two probes of the source meter.

I–V measurement was also performed with the freeze-dried scaffolds of the various SF/PEDOT-based ECHs within a potential sweep from −1 to +1 V to differentiate the inherent electronic conductivity of PEDOT:PSS from the ionic contribution, that observed in case of the hydrogel samples. The conductive ability of the ECH samples was also tested by powering a blue LED (50–70 mW) through them using a breadboard setup. All measurements were carried out for at least $n = 3$ samples per group.

2.5.6 | Electrochemical Impedance Spectroscopy (EIS)

Samples were prepared for EIS by applying 20 μL of each gel to a polished glassy carbon (GC) electrode with an inner diameter of 3 mm. Swagelok three-electrode cells were assembled using the as-prepared gel on GC as working electrode; YP-50 activated carbon (Kuraray) with 10% polytetrafluoroethylene (PTFE) binder (Sigma) as the counter electrode; Ag/AgCl as the reference electrode; cellulose filter membrane (Whatman) as the separator; and 10× PBS (Fisher) as the electrolyte. EIS spectra were obtained using a BioLogic VMP 300 potentiostat at open circuit voltage, from 1 Hz to 100 kHz, averaging three points per frequency, with an amplitude of 10 mV.

2.5.7 | Enzymatic Degradation Study

In vitro biodegradation behavior of the silk-based conductive hydrogels was evaluated in presence of protease XIV from *Streptomyces griseus* (Sigma-Aldrich, ≥ 3.5 U mg^{-1}) at 37°C to determine their stability in physiological conditions. Protease XIV can effectively break down the β-sheet crystalline structures in SF and therefore, widely used for assessing biodegradation of silk-based biomaterials [19]. In brief, various hydrogel samples were incubated in PBS with 2 U mL^{-1} of protease XIV in a 35 × 10 mm Petri dish separately. The initial weight of each hydrogel sample along with the Petri dish (excluding the proteolytic solution) was recorded. The experiment lasted until Day 31, with the enzyme solution being refreshed at every 3 days. During each solution change, the weight of each sample (including the vial) was recorded after rinsing the hydrogel samples with distilled water very carefully. Care was taken to prevent any mass loss due to mechanical stress during handling. For instance, forceps were not used to lift the hydrogel; instead, after washing the hydrogel, the remaining solvent was gently absorbed using tissue paper to minimize damage.

The percentage of remaining mass after incubation was calculated using the following formula:

$$\%\,\text{Mass remaining} = \text{Initial mass} - \frac{\text{Mass in time}'t'\ (\text{in mg})}{\text{Initial mass}} \times 100\,\%$$

A control study by incubating the hydrogel samples in phosphate buffer saline (PBS, pH = 7.4) at 37°C was carried out simultaneously for the same period and mass loss profile was evaluated.

2.5.8 | Swelling Study and Microstructural Evaluation

Swelling ratio is an important parameter, which indicates hydrogel network hydrophilicity as well as relative cross-linking density. Mass swelling ratio of different silk-based hydrogels were determined following a protocol described by Caliari et al. [77]. In summary, all hydrogel samples were incubated in 1× PBS (pH 7.4) at 37°C for 24 h to achieve equilibrium swelling. The wet weight (M_w) was then recorded after gently removing the excess solvent. The hydrogel samples were subsequently lyophilized, and the dry weight (M_d) was measured. The mass swelling ratio was calculated, which is defined as M_w/M_d. Subsequently, the microstructure of the lyophilized hydrogel scaffolds was assessed using scanning electron microscopy (Zeiss ULTRA plus) to correlate the observed swelling property.

2.6 | Cell Culture

2.6.1 | C3H10 Cell Culture

C3H10 T1/2, Clone 8, mouse embryonic fibroblasts were obtained from ATCC. The cells were cultured in growth media consisting of low-glucose DMEM with 10% v/v FBS and 2% v/v Pen-Strep, maintained at 37°C with 5% CO_2. The cells were passaged every 3 days or upon reaching 80% confluency.

2.6.2 | Human iPSC Neuronal Culture

The human iPSC line, KOLF2.1J used in this study was purchased from the Jackson Laboratory [78]. Culturing of iPSC prior to differentiation was performed on vitronectin (VTN; 0.5 μg cm^{-2}; Thermo Fisher Scientific, USA) with complete Essential 8TM flex media (E8; Thermo Fisher Scientific, USA). Detachment for passaging and seeding was accomplished using ethylenediaminetetraacetic acid (EDTA; 0.5 mM; 1 mL; Thermo Fisher Scientific, USA) [13]. iPSCs were patterned toward a cortical fate as previously described, using neural maintenance media (NMM, full composition in the Table S1) supplemented with SMAD inhibitors SB431542 (10 μM; Bio-Techne, USA) and LDN193189 (100 nM; Sigma-Aldrich, UK) for 10 days [10–12]. The NPC population at present is maintained in NMM following the initial passaging on Day 11 onto poly-L-ornithine/laminin-coated plate. Between Day 11 and 20, the NPCs are confirmed as a pure neuronal population through immunocytochemistry. Cortical neurons were derived by culturing NPCs in a six-well plate without passaging for 2 weeks. Following this period, the cortical neurons were ready for experimentation. In this study, cortical neurons from Day 50 to Day 60 cultures were utilized.

For cortical astrocytes, the NPC population cultured in NMM from Day 30 was subjected to cortical astrocyte progenitor patterning. This is accomplished by changing the media to ASTRO media (full composition in the Table S2) supplemented with epidermal growth factor (EGF, 20 ng/mL; Sigma-Aldrich, UK) and human leukemia inhibitory factor (hLIF, 20 ng mL^{-1}; Novus Biologicals) and passaging onto Geltrex (1×; Thermo Fisher Scientific, USA) plates [9]. Terminal differentiation to mature cortical astrocytes takes place from Day 80 to Day 120. This process involves replacing the EGF and LIF containing ASTRO media to ASTRO media supplemented with BMP4 (20 ng mL^{-1}; BioLegend) and hLIF (20 ng mL^{-1}) for 7 days followed by 3 days in ASTRO media without factors. After this 10-day process, mature cortical astrocytes were used for experimentation with the hydrogels.

2.7 | Live/Dead Assay

Preliminary biocompatibility of SF/PEDOT06, SF/PEDOT06*GoP*, and SF/PEDOT06*PeG* was tested by seeding C3H10 cells on the surface of hydrogels at a density of 2×10^5 cells/well. Pristine SF solution as well as the different PEDOT:PSS variants were sterilized by autoclaving them for 15 min, followed by 1 h of UV treatment. For cell seeding on the surface, a thin hydrogel layer was formed over a cover slip of 10 mm diameter (thickness: 0.13 mm). C3H10 cells were also encapsulated within different hydrogel samples at density of 2×10^7 cells/mL and deposited over a 10 mm cover slip (thickness: 0.13 mm). Viability of cells seeded on the surface and encapsulated within the hydrogels was assessed by live/dead assay after 3 and 6 days of culture, respectively. Cells were stained using 2 μL/mL EMA and 0.5 μL mL^{-1} calcein AM in PBS, followed by an incubation for 45 min at 37°C and 5% CO_2.

Live/dead staining was also performed to determine the viability of hiPSC-derived neurons and astrocytes, embedded in different hydrogel samples over 3 days. Matured iPSC-derived astrocytes and neurons were encapsulated within different hydrogels at densities of 3×10^7 and 2×10^6 cells mL^{-1}, respectively. Live/dead imaging was acquired using Olympus fluorescent microscope.

2.8 | β(III) Tubulin Immunostaining

To confirm the typical neuronal characteristics including visualization of development of axon and dendrites of the matured iPSC-derived neurons encapsulated within various ECHs, cells were stained using neuronal marker- anti-β(III) tubulin (BL-801202, BioLegend) after 7 days of culture. Thin hydrogel layers were prepared on cover slips (Karl Hecht Cover Slips, 12 mm diameter, 0.13 mm thickness), with cells embedded in them. The samples were rinsed with 1× PBS thrice and fixed with 4% paraformaldehyde (PFA) for 25 min at room temperature, followed by washing with PBS. The cells were blocked and permeabilized using 10% FBS in PBS containing 0.3% (v/v) Triton X-100 (Sigma-Aldrich) for 2 h. Cell laden ECHs were incubated with 5 μg/mL of anti-β(III) tubulin (1:1000) using 2% BSA in 1× PBS containing 0.06% Triton X-100 and incubated at 4°C for overnight. Subsequently, the samples were washed three times for 10 min each with PBST (1× PBS containing 0.02% Triton X-100), followed by incubation with 4 μg/mL of secondary antibody goat anti-mouse IgG H&L Alexa Fluor 488 (Abcam, ab150113) in PBST for 2 h in the dark at room temperature. Cells were counterstained with 1 μg/mL of DAPI (1:2000) in PBST for nucleus for 15 min. Once the staining process was completed, cell laden hydrogels together with the coverslips were mounted on glass slide and fixed using prolong gold anti-fade solution and were visualized under a Leica SP8 scanning confocal microscope and representative images are presented.

2.9 | Statistical Analysis

All tests with a minimum of $n = 3$ were replicated. Statistical analysis was performed using GraphPad Prism 10 software. Students *t*-test, One-way or two-way analysis of variance (ANOVA) analysis were used where appropriate to evaluate the statistical significance. For multiple comparisons, Tukey's test was performed along with ANOVA. Statistical significance was defined at $p < 0.05$. Results are presented as mean ± standard deviation (SD) or mean ± standard error of the mean (SEM).

3 | Results and Discussion

3.1 | Fabrication of SF/PEDOT:PSS Based Injectable Conductive Biomimetic Hydrogel

The main goal of this study was to develop a highly conductive hydrogel, mechanically robust yet flexible, that has suitable bioactivity to facilitate the formation of functional neuronal networks among encapsulated iPSC-derived neurons. For this, we chose highly bioactive SF blended with electroconductive PEDOT:PSS to fabricate an injectable ECH. There are practical concerns associated with hydrophilic PSS chains in PEDOT:PSS, which can be degraded or dissociated from PEDOT chains under aqueous environment, causing cytotoxic effects [37, 63, 73]. Hence, PEDOT:PSS was modified by 3% (v/v) GoPS and PeGDE (Figure 1A). The incorporation of GoPS into PEDOT:PSS was confirmed from the GoPS specific vibrational band around 1100 cm^{-1} (Si—O—Si) in the FT-IR spectra of PEDOT*GoP* (Figure S2) [79], while the strong peaks at 2872 and 1081 cm^{-1} corresponding to —CH stretching and ether bonds showed successful modification of PEDOT:PSS with PeGDE (Figure S2) [62].

SF, owing to its unique composition of large hydrophobic domains separated by smaller hydrophilic regions, can undergo self-assembly of the hydrophobic domains under temperature change and thus form parallel/antiparallel β sheets leading to in situ gelation [57, 58]. SF has previously been demonstrated to undergo accelerated gelation when blended with an anionic or a negatively charged agent, or an amphiphile such as tanic acid [80], sodium dodecyl sulfate (SDS) [74], and sophorolipid [72, 81]. PEDOT:PSS exhibits similar chemical characteristics, in addition to conductivity, with hydrophobic PEDOT chains and hydrophilic PSS, which is also negatively charged due to sulfonate groups (SO_3^-). Therefore, SF was observed to gel faster

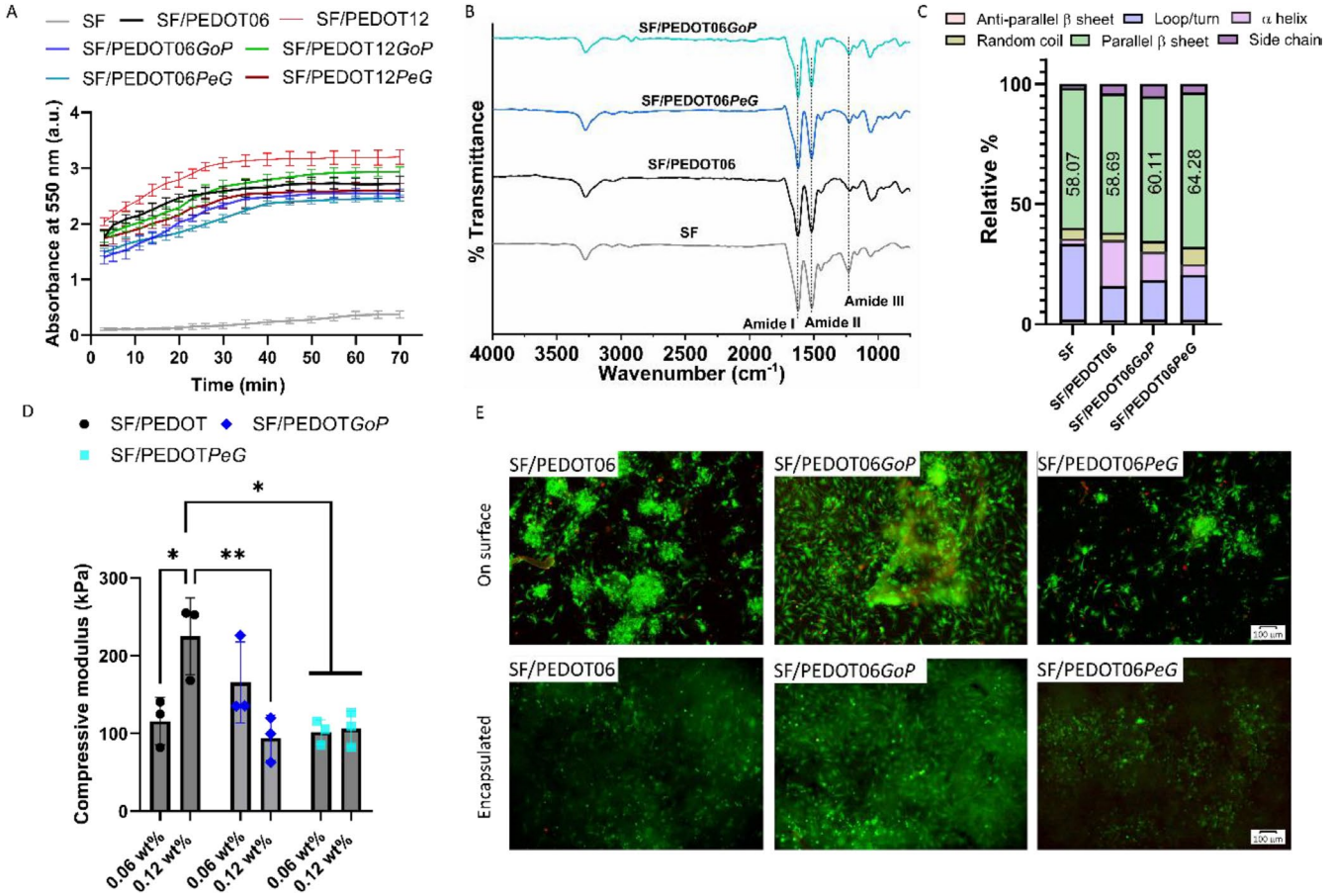

FIGURE 2 | Physicochemical and biocompatibility of silk-based ECHs. (A) Gelation kinetics at physiological conditions (37°C, neutral pH) presented in terms of absorbance displayed by different silk-based hydrogels with time. (B) FT-IR spectra of freeze-dried scaffolds of pure silk hydrogel and different variants of ECHs, as indicated. (C) Amide I peak deconvolution results showing relative percent of various silk fibroin secondary structures, as labeled (parallel β sheet content is highlighted). (D) Mechanical property of different ECHs with 0.06 and 0.12 wt% of PE, showing their compressive modulus (elastic modulus). (E) Live/dead imaging results showing viability of C3H10 cells, cultured on the surface of different ECHs for 3 days (upper panel) and embedded within the gels after 6 days (lower panel). Live and dead cells appear green and red, respectively. $^{**}p \leq 0.01$ and $^{*}p \leq 0.05$ in (D). Data were mean ± SD ($n = 3$). Scale bar = 100 μm (E).

when blended with different variants of PEDOT:PSS at 37°C, when compared to pristine SF (Figure 2A). In fact, gelation occurs instantly under low pH conditions. Commercially available PEDOT:PSS variants are generally acidic in nature (pH < 4). The addition of acidic PEDOT:PSS enhances the protonation of lysine residues in SF. This, in turn, strengthens the electrostatic interactions between the protonated amino groups of SF and the negatively charged sulfonate groups of PSS in PEDOT:PSS. As a result, highly inhomogeneous, phase-separated hydrogels are formed, which are not practically injectable (Figure S3). Therefore, the pH of the different PE variants was neutralized by adding NaOH prior to mixing with SF solution, which allows sufficient timeframe to achieve a uniform, homogeneous SF/PEDOT hydrogel (Figure 1B). The potential reason for this delayed gelation could be decreased protonation of lysine residues. While these residues can still interact electrostatically with the SO_3^- groups of PSS, the interaction is less extensive compared to that under acidic conditions. Furthermore, the partial deprotonation of carboxylic groups in SF might cause electrostatic repulsion with the negatively charged PSS chains, potentially delaying the hydrophobic interactions required for gelation for approximately 20 min. The silk blends with various PEDOT:PSS variants formed gels after being incubated at 37°C for 20 min, as confirmed by the inversion test (Figure 1C). This is also consistent with gelation kinetics study that indicated the initiation of gelation process of SF/PEDOT formulations at 5–11 min after mixing (Table S3). Additionally, the resulting ECHs exhibit good injectability when tested with a 22 G needle. However, SF/PEDOT*PeG* ECHs appeared to be softer as compared to the other variants after 20 min (during inversion test), potentially due to the delayed gelation kinetics (Figure 2A, Table S3). An important observation from the gelation kinetics study was that; similar to previously reported amphiphiles, various PEDOT:PSS variants also induced accelerated gelation of SF even at neutral pH. All SF/PEDOT formulations started gelation approximately 5–11 min after mixing, with the process concluding within 30–45 min as indicated by saturated absorbance (Figure 2A, Table S3). In contrast, the gelation time was approximately 35 min in pristine SF solution (3 wt%), before achieving maximum absorbance at around 60 min.

The major constituent of the ECHs was found to be SF, as evidenced by the FT-IR spectra of the various ECHs, which displayed strong characteristic SF bands for amide I, II, and III cantered around 1620, 1513, and 1235 cm^{-1}, respectively (Figure 2B) [82]. Particularly, the appearance of strong band at 1620 cm^{-1} in all the ECHs corresponds to the β-sheet of SF, indicating successful gelation [57]. Conversely, characteristic peaks for PEDOT:PSS, such as C═C stretching in the thiophene ring of PEDOT (~1502–1557 cm^{-1}), C═C stretching in the aromatic rings of PSS (~1601–1659 cm^{-1}), and symmetric and antisymmetric stretching of S═O (~1162 and ~1059 cm^{-1}, respectively) [83–85], seen in the FT-IR spectra of different PEDOT:PSS variants (Figure S2), mostly overlapped with the SF peaks in the FT-IR spectra of the ECHs (Figure 2B) [82]. The effect of accelerated gelation on the secondary structures of SF, due to the addition of different PEDOT:PSS variants, was assessed through peak deconvolution of the highly sensitive amide I region (Figure S4). The relative percentages of various secondary structures are presented in Figure 2C. The results show a relatively higher β-sheet content (~60%–66%) in the different ECHs compared to pure SF (~59%). Additionally, the ECHs with modified PEDOT:PSS variants (SF/PEDOT06*GoP* and SF/PEDOT06*PeG*) exhibited higher β-sheet content compared to SF/PEDOT06. Interestingly, the relative percentage of α-helices was reduced in the ECHs with modified PEDOT:PSS variants. Thus, the increase in β-sheet content and reduction in α-helices content collectively suggest improved gelation in terms of homogeneity and uniformity of the resulting ECHs. This has particular implications in the flow behavior of the ECHs, which is discussed in the subsequent sections. Although the relative β-sheet percentage in the ECHs with modified PEDOT:PSS variants was higher, we did not observe an increase in their stiffness constant or compressive fus compared to the ECHs with unmodified PEDOT: PSS (Figure 2D). This finding contrasts with previous reports suggesting that an increase in β-sheet content correlates with enhanced stiffness [86]. However, overall, all ECH variants exhibited significantly higher compressive modulus (~100–230 kPa) than pure silk hydrogel (~42.94 ± 13.11 kPa) (Figure S5), which also had higher β-sheet content, aligning with previous findings [86]. The discrepancy between the FT-IR analysis and compression test results likely arises from the different types of samples used for these analyses. FT-IR measurements were conducted on freeze-dried hydrogel scaffolds, while compression tests were performed on hydrogel samples 1 hour post-gelation. The reduced compressive modulus of the ECHs with GoPS modified PEDOT:PSS variants also indicated improved flexibility, which is essential for good injectability. As mentioned earlier, our goal is to develop a mechanically robust yet flexible conductive biomimetic hydrogel that can support the formation of neuronal networks by embedding iPSC-derived neuronal cells. Given that neuronal differentiation of iPSCs is complex, time-consuming, and expensive, it is essential to first assess the biocompatibility of the materials. To this end, we cultured C3H10 mouse embryonic fibroblasts on the surface of different ECH variants and assessed cell viability using live/dead staining after 3 days (upper panel in Figure 2E). Representative live/dead images show elongated and spreading morphology of fibroblasts on SF/PEDOT06*GoP* and SF/PEDOT06, while the cells on SF/PEDOT06*PeG* appeared round and stressed. Additionally, live/dead imaging results revealed that cells encapsulated within the ECHs showed healthier, spreading morphology in SF/PEDOT06*GoP* compared to SF/PEDOT06*PeG*, with SF/PEDOT06 demonstrating slightly better cell behavior overall (lower panel in Figure 2E). The findings highlight the potential toxicity issue associated with SF/PEDOT06*PeG* group, while some other reports suggested low cytotoxicity or improved cell viability of PeGDE cross-linked conductive scaffolds including PEDOT:PSS [62, 87]. Studies that reported improved cell viability typically evaluate PeGDE cross-linked PEDOT:PSS dry scaffolds, noting their enhanced hydrophilicity. In contrast, the present study uses SF/PEDOT*PeG* hydrogels, where PeGDE may become more reactive in a hydrated environment, potentially leading to undesirable side reactions and increased cytotoxicity. This explanation is consistent with previous research that has highlighted the potential toxic effects of PeGDE-based hydrogels [88, 89].

3.2 | Mechanical Stability

The ECHs are intended to be used for long-term culture of iPSC-derived neurons to evaluate their potential for SCR in a minimally invasive manner. This application requires the hydrogel network to maintain integrity and mechanical stability

in aqueous (cell culture media) conditions. Previous studies have shown that the strength and structure of SF can be compromised in aqueous environments [90]. Though this impact is minimal in the case of silk scaffolds, hydrogels are more susceptible to changes in mechanical strength due to their relatively softer nature and swelling behavior. Cheng et al. highlighted that water molecules weaken the hydrogen bonding between the β-sheets in the crystalline regions of SF, leading to a weaker and more brittle SF structure [91]. Indeed, any significant change in mechanical behavior can ultimately affect the conductive network. Therefore, a uniaxial unconfined compression test was conducted on various silk-based hydrogels before and after a 24-h incubation in PBS. As expected, all hydrogel samples, including pure silk hydrogel, exhibited a decrease in both compressive modulus (Figure 3A,B) and strength (Figure S5) after PBS incubation. Post-treatment, all ECHs retained compressive modulus and strength in the range of 25–110 kPa (Figure 3B) and 170–215 kPa (Figure S6), respectively. The compressive strength of pure silk hydrogel decreased from 194.64 ± 30.38 to 78.60 ± 34.87 kPa, and the compressive modulus also significantly dropped from 42.94 ± 13.11 to 16.34 ± 5.75 kPa (Figure S5). The results suggest that even after PBS treatment, all ECHs,

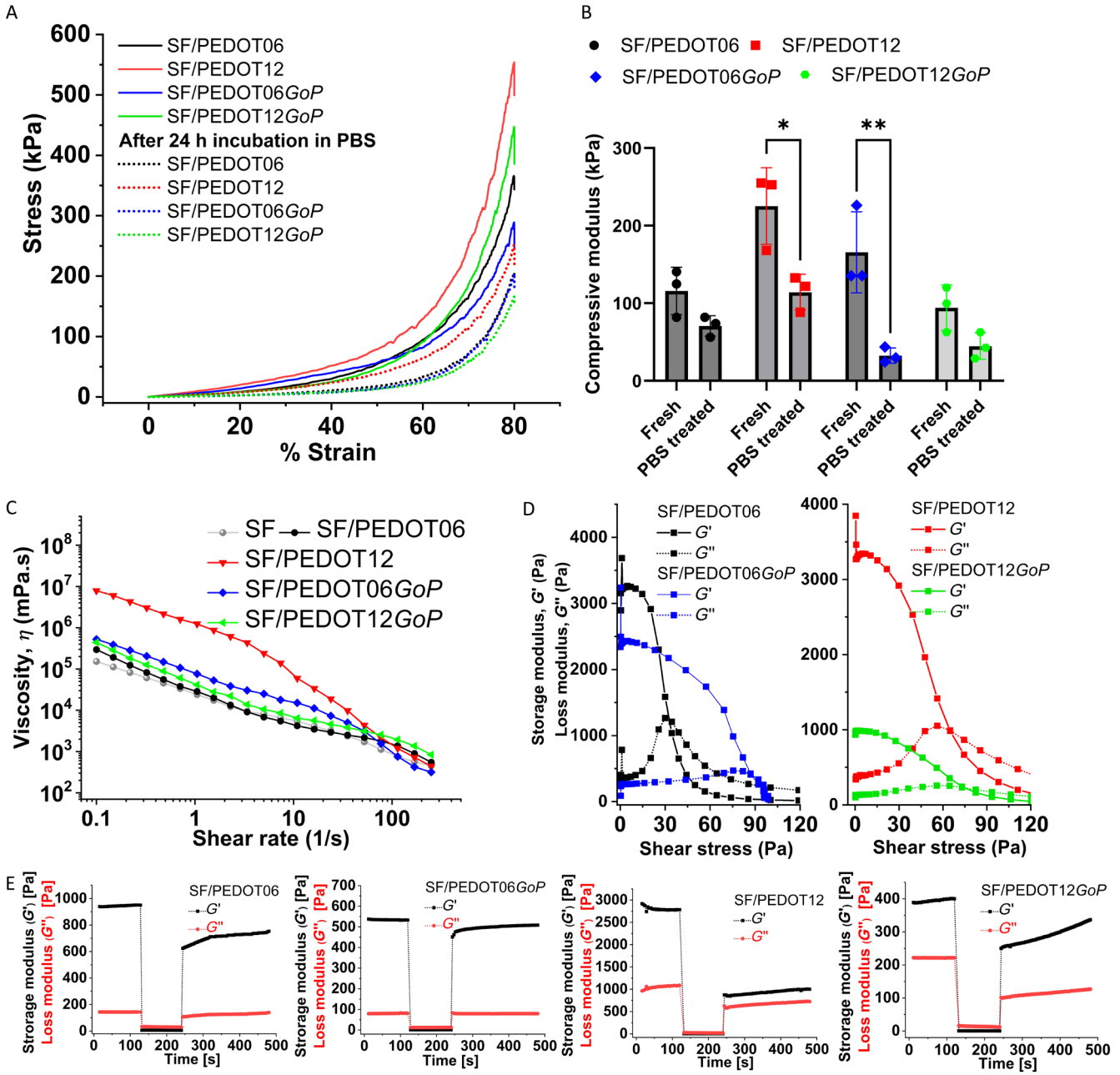

FIGURE 3 | Mechanical stability and rheological behavior. (A) Representative stress versus strain curves and (B) the corresponding compressive moduli of various silk-based ECHs before and after incubation in PBS for 24 h. (C) Viscosity test results showing shear-thinning property with increasing shear rate; (D) Amplitude sweep showing the change in the storage (G') and loss (G'') modulus of the silk-based hydrogels with applied stress. (E) Three interval time thixotropy (3ITT) test results depicting the dynamic viscoelastic behavior of the ECHs under low to high shear stress and structural recoverability features. $^{**}p \leq 0.01$ and $^{*}p \leq 0.05$ in (B). Data were mean ± SD ($n = 3$).

except SF/PEDOT12, maintain comparable elastic modulus similar to spinal cord or neural tissue (10–60 kPa) [18, 92]. While silk hydrogels retain similar elasticity, their structural integrity was completely compromised during the compression test, in contrast to the relatively intact hydrogel structures of the ECHs (Figure S7). The enhanced mechanical stability of the ECHs compared to pure silk hydrogels can be ascribed to the potential electrostatic interactions between the negatively charged PSS groups of PEDOT:PSS and the protonated amino groups of SF, which contribute to the structural integrity of the hydrogel network.

3.3 | Rheological Behavior

Rheological studies shows that the viscosity of different silk-based hydrogels decreased with increasing shear rate, indicating their non-Newtonian shear-thinning property and thereby, validates their injectability in a minimally invasive manner (Figure 3C). Although the viscosity of the different ECHs were higher than pure silk hydrogel, all of them, except SF/PEDOT12, showed similar shear-thinning behavior with increased shear rate. The viscoelastic nature and flow point of different ECHs were assessed with the help of amplitude measurement (Figure 3D). The ECHs with unmodified PEDOT:PSS variants exhibited a higher storage modulus (3000–3500 Pa) compared to those with modified PEDOT:PSS variants (1000–2500 Pa). This finding aligns well with the compression testing results, which demonstrated that SF/PEDOT06 and SF/PEDOT12 are stiffer (higher modulus) and tougher (higher compressive strength) than SF/PEDOT06*GoP* and SF/PEDOT12*GoP*. Notably, the ECHs with GoPS-modified PEDOT:PSS displayed a larger linear viscoelastic region (LVR) ($10 < \text{LVR} > 15$ Pa) compared to the unmodified versions ($0 < \text{LVR} < 10$ Pa). A larger LVR indicates that these hydrogels can withstand greater strains or stresses while maintaining their viscoelastic properties. Practically, this means the modified ECHs can undergo more deformation without deviating from their linear viscoelastic behavior, indicating greater flexibility. This is further supported by the compression study, which suggested a lower elastic modulus for the ECHs with GoPS-modified PEDOT:PSS. However, after a certain applied stress, both storage modulus (G') and loss modulus (G'') started to deviate from LVR and intersects each other at an applied stress below 100 Pa (Figure 3D). This intersection or cross over point of G' and G'' is called flow point, at which a viscoelastic solid start to display its liquid like flow behavior. Practically, it is a measure of stress necessary to induce flow [76]. Both the shear-thinning and amplitude sweep suggest good injectability of the ECHs for minimally invasive applications. However, the hydrogel network undergoes structural breakdown under injection force, which can be accompanied by changes in chain orientation or disassembly of the polymer/hydrogel network. For an injectable hydrogel used in tissue repair applications, structural recovery is crucial. This ensures that the injected hydrogel remains localized at the injury site and potentially maintains the integrity of the cellular network when used for cell delivery applications. Therefore, the 3ITT test was employed to uncover the dynamic viscoelastic behavior under low to high shear stress. All ECHs exhibited viscoelastic solid gel-like behavior ($G' > G''$) under low shear stress during the first time interval (0–120 s) (Figure 3E). However, when subjected to a sudden increase in shear stress in the second time interval (120–240 s), they displayed fluid-like behavior ($G'' > G'$), confirming their observed shear-thinning property. In the third time interval (240–480 s), as the applied stress is slowly removed, all ECHs regained its solid gel structure causing again $G' > G''$. Indeed, the ECHs with GoPS modified PEDOT:PSS, demonstrated higher structural recoverability (~70%–90%) as compared to the unmodified versions of the ECHs (~30%–80%), when compared to their initial G' value. In fact, SF/PEDOT12, which had the highest stiffness constant (less flexibility), exhibited the lowest structural recoverability (~30%). The enhanced structural recoverability of the ECHs with GoPS modified PEDOT:PSS can be attributed to their increased flexibility, as revealed by compression test analysis. The representative injectability visual image of SF/PEDOT06GoP clearly showed the unform hydrogel thread ejected from a 22 G nozzle, validating its structural integrity after injection (Figure 1C). The 3ITT test also revealed the higher G' value for the unmodified versions of the ECHs as compared to their modified counterparts, and thus also once again validated the compression test results. While the compression test shows the purely elastic response of the hydrogel samples under significant deformation, the oscillatory test (amplitude sweep) provides insight into the viscoelastic properties under a small oscillatory shear, specifically the storage modulus (G'). All ECHs demonstrated a storage modulus (G') in the range of 1000–3000 Pa, which falls within the typical range for the normal spinal cord (100–3000 Pa) [93]. These SF/PEDOT-based ECHs exhibit greater mechanical resilience, as indicated by their higher storage modulus, compared to previously reported injectable hydrogels (~1000 Pa) used for SCR [16, 21]. At the same time, they demonstrated favorable flow properties, making them suitable for minimally invasive applications.

3.4 | Conductive Behavior

Room temperature current–voltage (I–V) measurement was performed to assess the electroconductive behavior of the various ECHs under a bias voltage ±1 V. The measurement was carried out with the hydrated hydrogel samples implying that the contribution of ionic conductivity in the I–V characteristics. This is evident as some current passing through the pure silk hydrogel (Figure 4A). However, all the ECHs displayed nonlinear I–V characteristics with significantly higher current values than the pure silk hydrogel. While electrons and holes are the primary charge carriers in traditional semiconductors, electrically conducting polymers (ECPs) have unique charge carriers-solitons, polarons, and bipolarons [94]. As a result, their charge transport behavior varies depending on the applied bias voltage. In PEDOT:PSS, polarons and bipolarons are the primary charge carriers, which are quasi-particles formed when an electron is removed or added to the polymer chain, creating localized charge states that contribute to its electrical conductivity [95]. ECPs, including PEDOT:PSS, are well-known for exhibiting nonlinear I–V characteristics due to their distinct charge transport mechanisms [96–99]. Previous studies have shown that ECPs display Ohmic behavior at

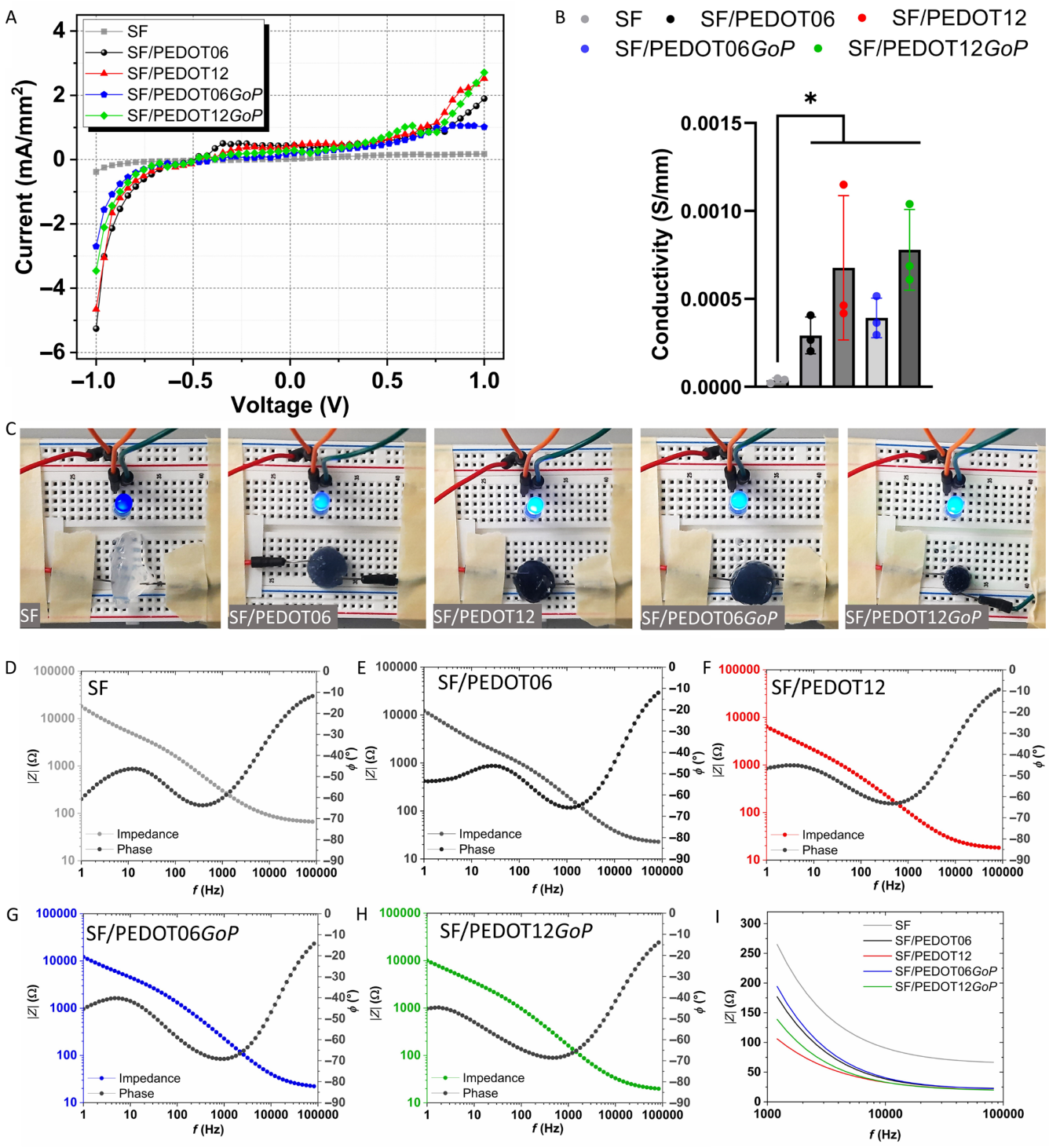

FIGURE 4 | Electrical conductivity and electrochemical impedance results. (A) Room temperature current–voltage (I–V) characteristics under a potential sweep from +1 to −1 V measured using a two probe set-up and (B) the conductivity values of various silk-based hydrogels derived from the I–V measurement. (C) Visual photographs showing ability of various hydrogel variants to transmit electrical signal through them by illuminating a blue LED (50–70 mW) using a power supply. Data were mean ± SD ($n = 3$) in (B); *$p \leq 0.05$. (D–H) Electrochemical impedance results showing Bode plots of various silk-based hydrogels as indicated. (I) High frequency impedance comparison of various silk-based conductive hydrogels including pristine SF.

low-voltage regions due to the higher density of intrinsic charge carriers compared to injected charge carrier density [99, 100], which is also observed in this case within the voltage range of approximately +0.5 to −0.5 V (Figure 4A). However, at higher voltages, the density of injected charge carriers becomes equivalent to the density of the thermally generated free carriers, causing the current to vary nonlinearly with voltage. This behavior follows the space-charge-limited conduction (SCLC)

mechanism due to trapped charges [99, 100]. PEDOT:PSS is well-known for exhibiting both ionic and electronic conductive behaviors [40, 41]. Therefore, at higher voltages, ion migration within the hydrated hydrogel environment can occur, leading to space-charge formation and electrochemical doping effects [40]. These factors can also contribute to the nonlinear I–V characteristics of these ECHs. Nevertheless, nonlinear behavior can still be observed in the I–V characteristics of the freeze-dried scaffolds of these ECHs (Figure S7), due to the distinct charge transport properties of ECPs.

Indeed, all the ECHs showed significantly higher conductivity ($>0.0002\,S\,mm^{-1}$ or $0.2\,S\,m^{-1}$), when compared to that of the pure silk hydrogel ($\sim0.001\,S\,m^{-1}$) (Figure 4B). Pure PEDOT:PSS hydrogels can exhibit conductivity as high as $\sim4000\,S\,m^{-1}$ [38], while PEDOT:PSS containing carbon nanotubes has a reported conductivity of $\sim2000\,S\,m^{-1}$ [39]. Most existing studies on highly conductive PEDOT-based hydrogels (without biopolymer components) require harsh chemical treatments, such as H_2SO_4 treatment, during fabrication to enhance conductivity. In contrast, the silk-based ECHs developed in this work use only water-based processing, offering a gentler and more environmentally friendly approach. These ECHs still demonstrates commendable conductivity in the range of $\sim0.2–1.2\,S\,m^{-1}$, which is much higher than previously reported biocompatible PEDOT:PSS/gelatin hydrogels ($\sim0.8\,\mu S\,cm^{-1}$) [48] or polyacrylamide/SF/PEDOT:PSS/graphene oxide hydrogels ($\sim0.085\,S\,m^{-1}$) [50]. The silk-based ECHs possess conductivity comparable to the conductivity of normal spinal cord ($1–10\,S\,m^{-1}$) [101], indicating their ability to mimic the native bioelectrical microenvironment. The ability to conduct electrical signal through these ECHs was further verified by illuminating a blue LED using a 3.3/5 V power supply (Figure 4C). The silk hydrogel, possessing minimal conductivity, resulted in very dim illumination of the blue LED, whereas the ECHs produced a bright illumination, highlighting their superior conductive properties. Although silk hydrogel prepared in deionized water, they showed some (ionic) conductivity, however, their freeze-dried scaffold counterparts exhibited no current flow implying their intrinsic insulating property (Inset of Figure S8).

EIS was used to probe the response of the various silk-based hydrogels at frequencies from 1 Hz to 100 kHz. In case of silk-based conductive hydrogels, impedance decreases dramatically with increasing PEDOT:PSS concentration, with SF hydrogel being notably more resistive than all others across the entire frequency range (Figure 4D–H). SF also showed the largest phase at 1 Hz, implying greater surface polarization at low frequencies, and being less efficient for electrostimulation [102]. At an electrophysiologically relevant frequency of 1000 Hz, impedance decreases approximately linearly with PEDOT:PSS concentration (Figure 4I). However, the modification of PEDOT:PSS with GoPS raises impedance relative to the ECHs containing unmodified PEDOT:PSS. Above 1000 Hz, the impedance converges for the ECHs with 0.06 and 0.12 wt% PEDOT:PSS, respectively, regardless of its modification with GoPS. This implies that GoPS has little to no negative effect on the intrinsic electrical conductivity of the hydrogels but may impact diffusional properties at lower frequencies due to the interconnected network of PSS chains.

3.5 | In Vitro Degradation Behavior, Swelling, and Microstructures of Silk-Based Conductive Hydrogels

We assessed the biodegradation characteristics of the various ECHs by simulating the physiological microenvironment with a protease solution over a period of 31 days. The enzymatic degradation behavior of the different silk-based hydrogels is shown as a percent of mass remaining at each time point as indicated (Figure 5A). The ECHs exhibited slower mass loss as compared to pure silk hydrogel. Pure silk hydrogel showed ~40% mass loss over 31 days under proteolytic condition, which is consistent with a previous report [57], while all ECHs demonstrated ~10% mass loss during the same period. The representative photographs of the degraded hydrogel samples are shown in Figure 5B after 31 days. Although the interaction mechanisms between SF and PEDOT:PSS were not explored in the present work, the negatively charged sulphonate group ($—SO_3^-$) of PSS in PEDOT:PSS is likely to electrostatically interact with the protonated lysine residues, resulting in a highly cross-linked network. Such tightly cross-linked network in the ECHs might prevent protease particles from cleaving the peptide bond in SF protein as reported earlier [103, 104]. This ultimately led to improved stability of the hydrogel architecture of the various ECHs, which is evident from Figure 5B. There is no difference observed in the degradation behavior of the unmodified ECHs and the ECHs with GoPS-modified PEDOT: PSS. Interestingly, the ECHs exhibited accelerated proteolytic degradation over the following 4 weeks, with over 50%–60% mass loss, while pure SF hydrogels showed nearly complete degradation (Figure S9). This accelerated degradation of ECHs after the initial 4 weeks aligns with previous studies on CNT-based conductive hydrogels [23]. The stability of the various ECHs, including pure silk hydrogel, was further confirmed by the observation of less than 5% mass loss after incubation in PBS (pH 7.4) at 37°C for 31 days (Figure S10). A key finding that underscores the exceptional stability of these ECHs is their current conduction ability, even after 31 days of incubation in PBS (Figure S11). The incubated ECHs maintained the ability to conduct approximately 0.2 mA of current, indicating their potential suitability for long-term cell culture applications under electrical stimulation, which is the primary objective in developing this ECH.

ECHs with unmodified PEDOT:PSS variants showed relatively lower swelling behavior when compared to the ECHs with modified PEDOT:PSS variants (Figure 5C), which can be attributed to their highly dense and low porous morphology as evidence by FESEM results (Figure 5D). The greater electrostatic interaction is assumed to induce tightly packed networks (with low porosity) as can be seen in FESEM images of SF/PEDOT06 and SF/PEDOT12. These tightly packed structures may prevent or limit the penetration of water molecules deep into the hydrogel network, leading to their slow degradation rate and reduced swelling behavior [105]. Additionally, the higher compressive strength (Figure S6) and modulus (Figure 3B) of SF/PEDOT06 and SF/PEDOT12 are supported by their dense tightly packed networks [105]. In contrast, in case of the GoPS-modified ECHs, the degree of such interactions might be limited. It is because GoPS was shown to interact with the highly active sulphonate groups ($—SO_3^-$) in PSS [79] leaving fewer active sites for electrostatic interaction with SF. This results in relatively larger

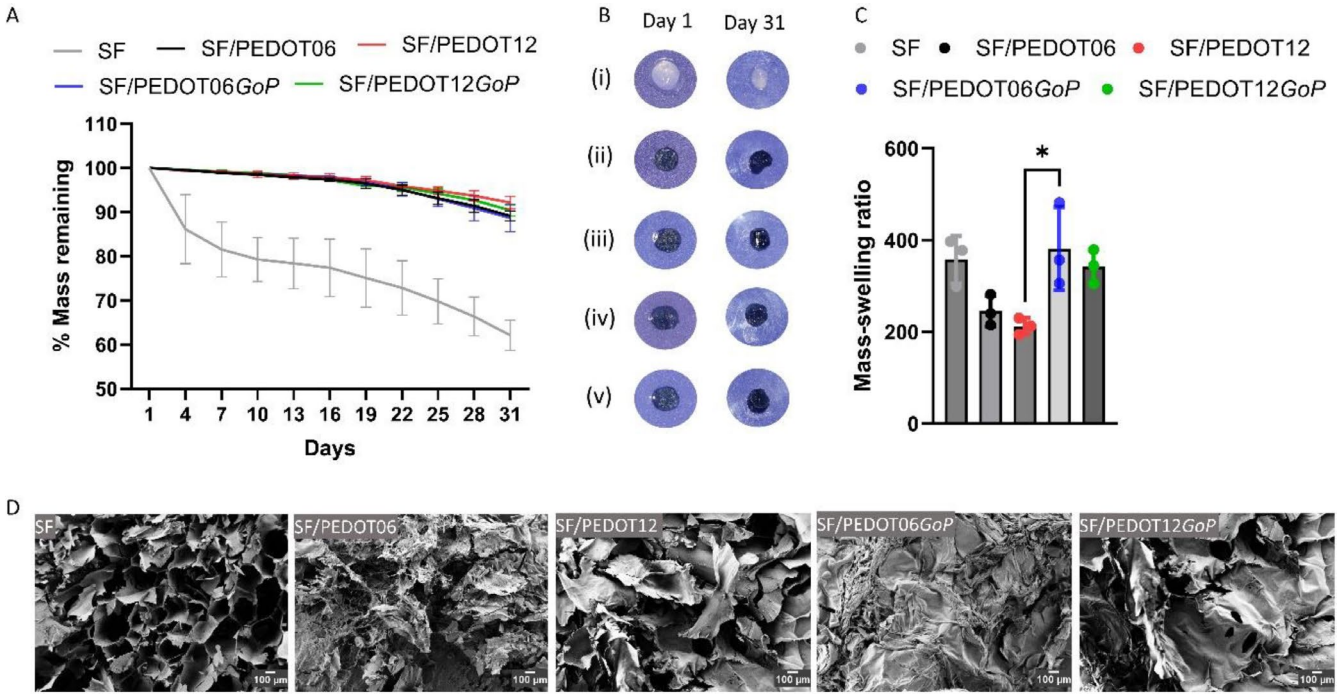

FIGURE 5 | Physicochemical characteristics of different silk-based hydrogels. (A) In vitro mass loss profile showing % mass remaining of different hydrogels under proteolytic condition at 37°C till 31 days [(i) SF, (ii) SF/PEDOT06, (iii) SF/PEDOT12, (iv) SF/PEDOT06GoP, and (v) SF/PEDOT12GoP]. (B) Representative photographs of the silk-based hydrogels before and after 31 days of incubation in proteolytic condition. (C) Mass swelling ratio and (D) scanning electron micrographs of various silk-based hydrogel samples (scale bar = 100 µm). Data were mean ± SD ($n = 3$) in (A and B); *$p \leq 0.05$.

pore sizes in SF/PEDOT06*GoP* and SF/PEDOT12*GoP*, which is supported by their increased swelling behavior along with lower compressive modulus and strength, as discussed above. However, a better understanding about the interaction mechanisms of SF with different PEDOT:PSS variants will be needed to validate these explanations.

3.6 | Viability of Encapsulated iPSC-Derived Neurons and Astrocytes

To reiterate, our goal is to develop injectable ECHs for potential applications in spinal cell transplantation and as a physical support to bridge lesions by integrating with the surrounding native tissue. Hence, it is essential to test the viability of the hiPSC-derived cortical neurons and glia embedded in the different silk-based ECHs. Most cell transplantation methods have traditionally struggled with poor viability, with reported survival rates as low as 1% [6]. Maintaining the viability of iPSC-derived differentiating neuronal cells within hydrogels is challenging because these cells are prone to undergoing cell death in the absence of proper cell adhesion through a process called anoikis (i.e., programmed cell death triggered by the lack of matrix attachment) [16]. Although amino acid sequence in SF is composed of a range of reactive amino acids, silk hydrogel has not been investigated with iPSC-derived neuronal cells yet. Therefore, we encapsulated hiPSC-derived mature cortical neurons and astrocytes within various silk-based ECH variants and assessed their viability after 3 days of culture using a live/dead assay. Representative live/dead imaging results of the both cell types showed a very high density of viable cells (green) as compared to few dead cells (red) in all of the silk-based ECH variants (Figure 6A,B). Quantitative analysis of the live/dead imaging results also demonstrated more than 80% of viability of both hiPSC-derived matured cortical neurons and astrocytes within the ECHs (Figure 6C,D). These ECHs demonstrated cell viability comparable to a 3D bioprinted fibrin hydrogel, which exhibits functional neuronal connectivity [8] and superior to a protein-engineered hydrogel proven effective in treating injured cervical spinal cord [16]. These SF/PEDOT-based ECHs exhibited superior cellular morphology and distribution of both hiPSC-derived cortical neurons and astrocytes compared to similar cells encapsulated in PEDOT:PSS hydrogel [56]. The presence of neurite projections within the various ECHs indicates the stability of the neuronal network integrity, suggesting their promising potential for spinal cell transplantation. The findings reveal that ECH variants with 0.06 wt% PEDOT:PSS or GoPS-modified PEDOT:PSS exhibited relatively higher cell viability and robust axonal projections compared to ECH with 0.12 wt% PEDOT:PSS (SF/PEDOT12), though the differences were not statistically significant. The ECHs with GoPS-modified PEDOT:PSS possessed soft microenvironment (storage modulus ~1000–2000 Pa), which was demonstrated previously for improved neuronal differentiation of NSCs [21]. Specifically, the lower stiffness and higher porosity of the GoPS-modified ECHs contributed to enhanced cell viability. Increased porosity with larger pore sizes facilitates the effective transport of nutrients and oxygen to the cells within the hydrogels, ensuring cell survival [8]. It is to be noted that pure SF hydrogel supported enhanced viability (> 80%) of cortical neurons and astrocytes when compared to that on PEDOT:PSS drop casted film (Figure S12). Astrocyte viability was approximately

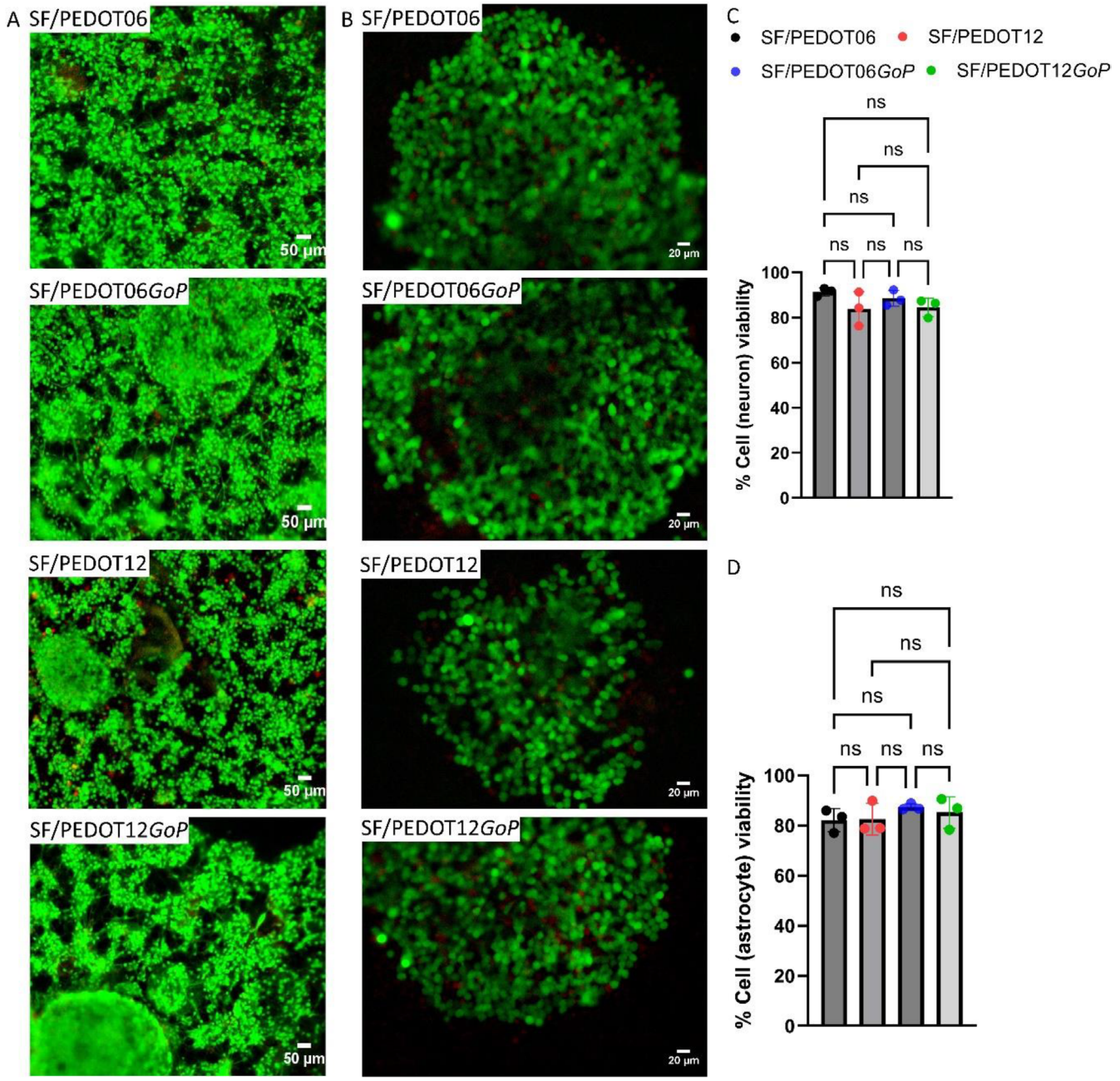

FIGURE 6 | Viability of matured cortical neurons and astrocytes encapsulated within silk-based ECHs. Representative live/dead images of (A) matured cortical neurons and (B) matured astrocytes grown within various ECHs for 3 days. Quantitative analysis of live/dead results showing percentage of viability of (C) matured cortical neurons and (D) matured astrocytes. No statistical significance exists and represented as "ns" in (C and D); Data were mean ± SD ($n = 3$). Scale bar in (A) 50 µm and (B) 20 µm.

65%, while around 75% of cortical neurons remained viable on the PEDOT:PSS film. This result suggest that inherent bioactivity of SF had a significant role in enhanced cellular viability within the ECHs. SF is a naturally derived protein composed of amino acid sequences that include several highly reactive amino acids such as lysine, tyrosine, serine, aspartic acid, and glutamic acid [61]. These amino acids can mimic native ECM interactions with cell surface integrins, thereby enhancing cellular adhesion and proliferation. In addition to SF chemistry, the interconnected porous structure of the various silk-based hydrogels contributed to enhanced cellular viability, consistent with previous studies [106, 107].

3.7 | Neural Network Formation

So far, we have demonstrated that silk-based injectable ECHs can support the viability of hiPSC-derived mature cortical neurons and astrocytes and provide preliminary evidence of maintaining axonal projections. Cell transplantation using mature cell types is more effective as it provides greater control over the final lineage commitment [7]. However, this approach is challenging because mature cells are more susceptible to changes in neuronal network formation efficiency during manipulations before transplantation [16]. To confirm typical neuronal features such as axonal growth and synapse formation by mature

cortical neurons within the ECH network, cells were immunostained after 7 days of culture with a neuronal marker, β(III) tubulin, which is a crucial microtubule component required for axon and dendrite development. Representative confocal images show the matured cortical neurons encapsulated in various ECHs expressed β(III) tubulin (green) throughout all the cell bodies (blue for nucleus) and axonal projections (Figure 7A). Importantly, the neurons extended elaborate axonal processes with extensive branching, forming a complex axonal network that interacted among themselves. The complexity of the neuronal network formed with these ECHs resembles that of the iPSC-derived neuronal networks reported in previous studies [8, 16, 108]. Many of the encapsulated neurons in these ECHs exhibited a pyramidal morphology (Figure 7B) suggesting their excitatory features [8], which play crucial role in transmitting signals and other synaptic functions. A functional neural network is also characterized by axonal branch development and synaptic plasticity [109, 110]. The encapsulated cortical neurons in the ECHs revealed extensive collateral branches from the axon shaft (Figure 7C). A functional neural network is also characterized by axonal branch development and synaptic plasticity [109, 110]. The encapsulated cortical neurons in the ECHs revealed extensive collateral branches from the axon shaft (Figure 7C). Collectively, the ECHs support the maturation of cortical neurons by fostering the development of a complex, interconnected network of long processes and promoting synaptogenesis. Indeed, the ECH formulation with the highest content of unmodified PE, specifically SF/PEDOT12, exhibited poorer neuronal network formation. This can be attributed to its higher stiffness (compressive modulus) and more compact hydrogel network with lower porosity, as demonstrated by the compression test and microstructural analysis discussed in the preceding sections. This explanation aligns well with previous studies, which have indicated that rigid gels limit functional connectivity among neurons [32, 111]. To further emphasize the visual observations, the confocal images were analyzed using ImageJ software for quantitative measurement of axonal length and branches as described previously [109, 110]. The total axonal lengths and number of axon collaterals (branches) were measured in five random regions of an ECH formulation. The data are

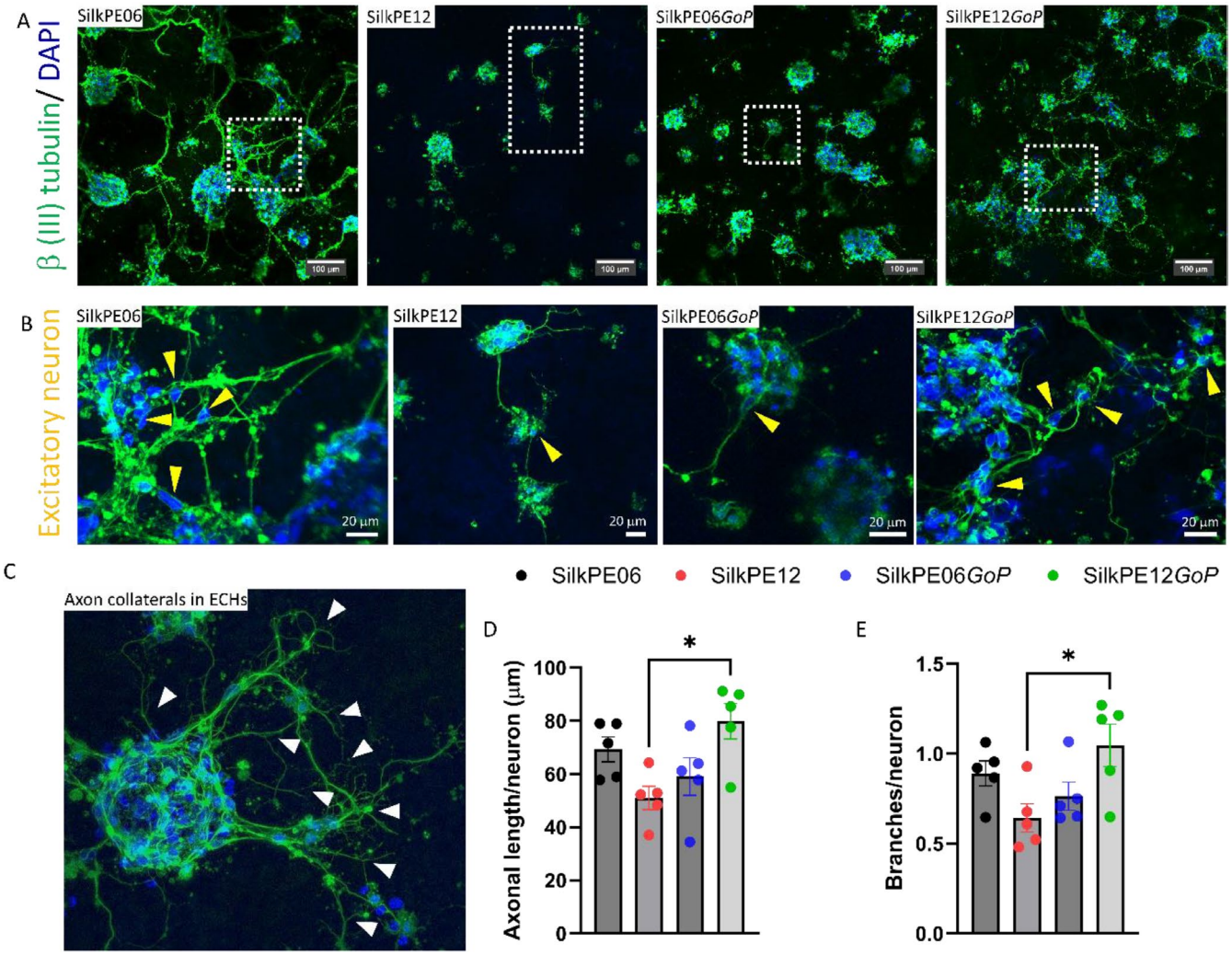

FIGURE 7 | Neuronal network formation within various ECHs. (A) β(III) tubulin immunostaining (green) of hiPSC-derived matured cortical neurons (DRGs) neurons, counterstained with DAPI for nucleus (blue), grown within various ECHs for 7 days; scale bar = 100 µm. (B) Zoomed confocal images highlighting pyramidal morphology of excitatory neurons (yellow arrowhead); scale bar = 20 µm. (C) A representative image of neuron (in SF/PEDOT06) showing axonal collaterals with white arrowhead. Quantitative assessment of β(III) tubulin immunostaining results showing (D) axonal length per neuron and (E) branching number per neuron. *$p \leq 0.05$; Data were mean ± SEM ($n = 5$).

presented as axonal length per neuron and number of branches per neuron (Figure 7D,E). The results showed the longest axonal projection and higher branching on SF/PEDOT12*GoP* followed by SF/PEDOT06. In contrast, SF/PEDOT12 exhibited shorter axonal projection and lower branching, aligning with the finding suggested by visual observation of β(III) tubulin stained images. The results are statistically significant between SF/PEDOT12 and SSF/PEDOT12*GoP*. Overall, the GoPS-modified ECHs showed enhanced neural network formation along with the ECHs with 0.6 wt% PE, that is, SF/PEDOT06. These ECH formulations exhibit nearly identical stiffness, porosity, and conductive behavior, indicating that these material properties play a crucial role in determining the efficiency of neuronal network formation and functional connectivity [8, 31, 32, 111]. Moreover, the encapsulated iPSC-derived neurons within these ECHs demonstrated superior axonal projections when compared to the iPSC neurons grown within a protein-engineered polymeric hydrogel, reported elsewhere [16]. Hence, apart from the bioactivity conferred by SF, interconnected porous morphology and compatible mechanical environment, the electroconductive microenvironment within the ECHs can offer better regulation of intracellular and extracellular Ca^{2+} dynamics for enhanced axonal projections in the cortical neurons. The increased intracellular Ca^{2+} signaling can activate downstream PI3K/AKT signaling pathway, which in turn promote CREB (cAMP response element-binding protein) and BDNF (brain derived neurotrophic factor) transcriptional expression, leading to enhanced axonal growth [22, 25]. Feig et al. were the first to demonstrate the viability of hiPSC-derived NPCs within a PEDOT:PSS hydrogel for up to 5 days [56]. In the present study, the SF/PEDOT:PSS based injectable ECHs, which were developed using cross-linker free strategy, supported the formation of a complex neural network by hiPSC-derived neurons, as well as the viability of hiPSC-derived astrocytes.

4 | Conclusions

In conclusion, the present study demonstrated a versatile, cross-linker free strategy to develop an injectable conductive hydrogel, both mechanically robust and flexible, which can support functional neural neuronal networks using encapsulated hiPSC-derived matured neurons. The ECH was prepared by blending bioactive SF with PEDOT:PSS, where self-assembly of hydrophobic domains of SF induce in situ gelation through hydrophobic–hydrophilic interactions at physiological temperature (37°C). The introduction of electroconductive PEDOT:PSS, makes the gelation process faster due to its amphiphilic nature. Accelerated gelation kinetics induced by various PEDOT:PSS variants was supported by the higher β-sheet content suggesting improved gelation homogeneity. The ECHs exhibited superior mechanical property than silk hydrogel, assessed in terms of compressive modulus, which is also comparable to spinal cord or neural tissue (~10–60 kPa) under physiological condition. The ECHs also demonstrated non-Newtonian shear-thinning properties, crucial for minimally invasive delivery. The flow point of these ECH formulations were below 100 Pa, indicating their potential injectability using a normal syringe with normal thumb pushing of an individual. The fabricated ECHs are electrically conductive, which was evidenced by their nonlinear I–V characteristics and bright illumination under a blue LED. hiPSC-derived cortical neurons and astrocytes embedded in the silk-based ECHs showed more than 80% cell viability, suggesting their potential integration with iPSC transplantation therapy for SCR. As indicated by β(III) tubulin immunostaining, the ECHs support the maturation of cortical neurons by fostering the development of a complex, interconnected network of long processes, and promoting synaptogenesis. Overall, this study provides strong evidence that silk-based ECHs can be effectively integrated with iPSC transplantation therapy, ensuring the viability of mature fate-restricted neurons within their hydrogel network. Additionally, these ECHs offer a native bioelectrical microenvironment that promotes increased excitatory activity among the neurons, ensuring a functional neural network. Given the multifaceted SCI pathophysiology characterized by various processes, including glial scar formation, vasculature disruption, sustained inflammation, cell death, growth factor deficiency, and so forth [3, 112–114], the present study is limited in assessing the material impact on cell viability and neuronal network formation only. To establish the ECHs developed in this study as a viable clinical option for SCI treatment, comprehensive evaluation is needed in an SCI-like microenvironment that involves complex interactions among the heterogeneous cell populations of the spinal cord, including neurons, astrocytes, microglia, and circulating macrophages, both in vitro and in vivo. Despite these limitations, the promising preliminary findings of the present study demonstrated a bioactive and conductive minimally invasive platform with potential applications in SCR. The next step involves assessing this minimally invasive platform in combination with hiPSC technology under exogenous wireless electrical stimulation, both in vitro and in vivo, using the capacitive coupling power transfer technique demonstrated recently [24].

Acknowledgments

This project has received funding from the European Union's Horizon 2020 Research and Innovation Programme under the Marie Skłodowska-Curie (Grant 101067283). M.G.M. and D.D.C. acknowledge CRY Ireland for Michael Greene Cardiac Risk in the Yong (CRY) summer scholarship (CRYUG/2023/001). The authors also acknowledge EPSRC and SFI Centre for Doctoral Training in Engineered Tissues for Discovery, Industry and Medicine, for funding this work (Grant EP/S02347X/1). R.B. acknowledges the help received from Dr. Manuel Ruether, Department of Chemistry, TCD and Dr. Jijo Thomas, Trinity Centre for Biomedical Engineering, TCD for FT-IR measurements and rheology tests, respectively. R.B. also would like to thank Robert Dunbar, Department of Mechanical, Manufacturing and Biomedical Engineering, TCD for the assistance during compression test. Scanning Electron Microscopy for this project was carried out at the Advanced Microscopy Laboratory (AML), Trinity College Dublin, Ireland. The AML (www.tcd.ie/crann/aml) is an SFI supported imaging and analysis centre, part of the CRANN Institute and affiliated to the AMBER centre. V.N. and D.S. wish to thank the support of the EIC Transition Grant Super-HEART (Grant 101057679), the Research Ireland-funded AMBER Research Centre, and Frontiers for the Future award (Grant Nos. 12/RC/2278_P2 and 20/FFP-A/8950, respectively).

Conflicts of Interest

The authors declare no conflicts of interest.

Data Availability Statement

The data that support the findings of this study can be obtained from the corresponding author upon reasonable request.

References

1. S. L. James, A. Theadom, R. G. Ellenbogen, et al., "Global, Regional, and National Burden of Traumatic Brain Injury and Spinal Cord Injury, 1990–2016: A Systematic Analysis for the Global Burden of Disease Study 2016," *Lancet Neurology* 18, no. 1 (2019): 56–87.

2. D. Sandean, "Management of Acute Spinal Cord Injury: A Summary of the Evidence Pertaining to the Acute Management, Operative and Non-Operative Management," *World Journal of Orthopedics* 11, no. 12 (2020): 573–583.

3. E. A. Kiyotake, M. D. Martin, and M. S. Detamore, "Regenerative Rehabilitation With Conductive Biomaterials for Spinal Cord Injury," *Acta Biomaterialia* 139 (2022): 43–64.

4. N. Hlavac, M. Kasper, and C. Schmidt, "Progress Toward Finding the Perfect Match: Hydrogels for Treatment of Central Nervous System Injury," *Materials Today Advances* 6 (2020): 100039.

5. M. Pitonak, M. Aceves, P. A. Kumar, et al., "Effects of Biological Sex Mismatch on Neural Progenitor Cell Transplantation for Spinal Cord Injury in Mice," *Nature Communications* 13, no. 1 (2022): 5380.

6. N. Mitrousis, A. Fokina, and M. S. Shoichet, "Biomaterials for Cell Transplantation," *Nature Reviews Materials* 3, no. 11 (2018): 441–456.

7. G. I. Nistor, M. O. Totoiu, N. Haque, M. K. Carpenter, and H. S. Keirstead, "Human Embryonic Stem Cells Differentiate Into Oligodendrocytes in High Purity and Myelinate After Spinal Cord Transplantation," *Glia* 49, no. 3 (2005): 385–396.

8. Y. Yan, X. Li, Y. Gao, et al., "3D Bioprinting of Human Neural Tissues With Functional Connectivity," *Cell Stem Cell* 31, no. 2 (2024): 260–274.

9. L. A. Crompton, S. F. McComish, P. Stathakos, O. Cordero-Llana, J. D. Lane, and M. A. Caldwell, "Efficient and Scalable Generation of Human Ventral Midbrain Astrocytes From Human-Induced Pluripotent Stem Cells," *JoVE (Journal of Visualized Experiments)* 176 (2021): e62095.

10. Y. Shi, P. Kirwan, and F. J. Livesey, "Directed Differentiation of Human Pluripotent Stem Cells to Cerebral Cortex Neurons and Neural Networks," *Nature Protocols* 7, no. 10 (2012): 1836–1846.

11. P. A. Nistor, P. W. May, F. Tamagnini, A. D. Randall, and M. A. Caldwell, "Long-Term Culture of Pluripotent Stem-Cell-Derived Human Neurons on Diamond—A Substrate for Neurodegeneration Research and Therapy," *Biomaterials* 61 (2015): 139–149.

12. S. M. Chambers, C. A. Fasano, E. P. Papapetrou, M. Tomishima, M. Sadelain, and L. Studer, "Highly Efficient Neural Conversion of Human ES and iPS Cells by Dual Inhibition of SMAD Signaling," *Nature Biotechnology* 27, no. 3 (2009): 275–280.

13. G. Chen, D. R. Gulbranson, Z. Hou, et al., "Chemically Defined Conditions for Human iPSC Derivation and Culture," *Nature Methods* 8, no. 5 (2011): 424–429.

14. M. J. Devine, M. Ryten, P. Vodicka, et al., "Parkinson's Disease Induced Pluripotent Stem Cells With Triplication of the α-Synuclein Locus," *Nature Communications* 2, no. 1 (2011): 440.

15. M. H. Amer, F. R. Rose, K. M. Shakesheff, M. Modo, and L. J. White, "Translational Considerations in Injectable Cell-Based Therapeutics for Neurological Applications: Concepts, Progress and Challenges," *Npj Regenerative Medicine* 2, no. 1 (2017): 23.

16. V. Doulames, L. Marquardt, M. Hefferon, et al., "Custom-Engineered Hydrogels for Delivery of Human iPSC-Derived Neurons Into the Injured Cervical Spinal Cord," *Biomaterials* 305 (2024): 122400.

17. J. Wang, R. Chu, N. Ni, and G. Nan, "The Effect of Matrigel as Scaffold Material for Neural Stem Cell Transplantation for Treating Spinal Cord Injury," *Scientific Reports* 10, no. 1 (2020): 2576.

18. C. M. Tringides, M. Boulingre, A. Khalil, T. Lungjangwa, R. Jaenisch, and D. J. Mooney, "Tunable Conductive Hydrogel Scaffolds for Neural Cell Differentiation," *Advanced Healthcare Materials* 12, no. 7 (2023): 2202221.

19. J. M. Das, J. Upadhyay, M. G. Monaghan, and R. Borah, "Impact of the Reduction Time-Dependent Electrical Conductivity of Graphene Nanoplatelet-Coated Aligned *Bombyx mori* Silk Scaffolds on Electrically Stimulated Axonal Growth," *ACS Applied Bio Materials* 7, no. 4 (2024): 2389–2401.

20. S. J. Peñas-Núñez, D. Mecerreyes, and M. Criado-Gonzalez, "Recent Advances and Developments in Injectable Conductive Polymer Gels for Bioelectronics," *ACS Applied Bio Materials* 7, no. 12 (2024): 7944–7964.

21. Y. Feng, Z. Yu, H. Liu, et al., "Biomimicking 3D Soft Scaffold Combined With Electrical Stimulation to Manipulate Neural Stem Cell Differentiation for Guidance Spinal Cord Injury Repair," *Materials Today* 71 (2023): 50–62.

22. P. Wu, P. Chen, C. Xu, et al., "Biodegradable Conductive Hydrogels Generating Magnetic-Field-Driven Wireless Electrical Stimulation Enhance the Spinal Cord Injury Repair," *Nano Energy* 130 (2024): 110123.

23. S. Yao, Y. Yang, C. Li, et al., "Axon-Like Aligned Conductive CNT/GelMA Hydrogel Fibers Combined With Electrical Stimulation for Spinal Cord Injury Recovery," *Bioactive Materials* 35 (2024): 534–548.

24. P. Wu, C. Xu, X. Zou, et al., "Capacitive-Coupling-Responsive Hydrogel Scaffolds Offering Wireless In Situ Electrical Stimulation Promotes Nerve Regeneration," *Advanced Materials* 36, no. 14 (2024): 2310483.

25. M. Liu, W. Zhang, S. Han, et al., "Multifunctional Conductive and Electrogenic Hydrogel Repaired Spinal Cord Injury via Immunoregulation and Enhancement of Neuronal Differentiation," *Advanced Materials* 36, no. 21 (2024): 2313672.

26. N. H. Shahemi, M. M. Mahat, N. A. N. Asri, M. A. Amir, S. Ab Rahim, and M. A. Kasri, "Application of Conductive Hydrogels on Spinal Cord Injury Repair: A Review," *ACS Biomaterials Science & Engineering* 9, no. 7 (2023): 4045–4085.

27. W. Kong, Y. Zhao, Y. Xiaoyu, et al., "Combined Treatment Using Novel Multifunctional MAu-GelMA Hydrogel Loaded With Neural Stem Cells and Electrical Stimulation Promotes Functional Recovery From Spinal Cord Injury," *Ceramics International* 49, no. 12 (2023): 20623–20636.

28. S. Santhanam, V. R. Feig, K. W. McConnell, et al., "Controlling the Stem Cell Environment via Conducting Polymer Hydrogels to Enhance Therapeutic Potential," *Advanced Materials Technologies* 8, no. 10 (2023): 2201724.

29. C. Wu, S. Chen, T. Zhou, et al., "Antioxidative and Conductive Nanoparticles-Embedded Cell Niche for Neural Differentiation and Spinal Cord Injury Repair," *ACS Applied Materials & Interfaces* 13, no. 44 (2021): 52346–52361.

30. T. Liu, Q. Zhang, H. Li, X. Cui, Z. Qi, and X. Yang, "An Injectable, Self-Healing, Electroconductive Hydrogel Loaded With Neural Stem Cells and Donepezil for Enhancing Local Therapy Effect of Spinal Cord Injury," *Journal of Biological Engineering* 17, no. 1 (2023): 48.

31. R. Lozano, L. Stevens, B. C. Thompson, et al., "3D Printing of Layered Brain-Like Structures Using Peptide Modified Gellan Gum Substrates," *Biomaterials* 67 (2015): 264–273.

32. M. A. Skylar-Scott, J. Y. Huang, A. Lu, et al., "Orthogonally Induced Differentiation of Stem Cells for the Programmatic Patterning of Vascularized Organoids and Bioprinted Tissues," *Nature Biomedical Engineering* 6, no. 4 (2022): 449–462.

33. B. Oh, Y. W. Wu, V. Swaminathan, V. Lam, J. Ding, and P. M. George, "Modulating the Electrical and Mechanical Microenvironment to Guide Neuronal Stem Cell Differentiation," *Advanced Science* 8, no. 7 (2021): 2002112.

34. F. F. Garrudo, D. E. Nogueira, C. A. Rodrigues, et al., "Electrical Stimulation of Neural-Differentiating iPSCs on Novel Coaxial

Electroconductive Nanofibers," *Biomaterials Science* 9, no. 15 (2021): 5359–5382.

35. J. Liu, T. Zou, Y. Zhang, et al., "Three-Dimensional Electroconductive Carbon Nanotube-Based Hydrogel Scaffolds Enhance Neural Differentiation of Stem Cells From Apical Papilla," *Biomaterials Advances* 138 (2022): 212868.

36. H. He and J. Ouyang, "Enhancements in the Mechanical Stretchability and Thermoelectric Properties of PEDOT:PSS for Flexible Electronics Applications," *Accounts of Materials Research* 1, no. 2 (2020): 146–157.

37. C. Yu, Z. Yue, H. Zhang, et al., "Ultra-Histocompatible and Electrophysiological-Adapted PEDOT-Based Hydrogels Designed for Cardiac Repair," *Advanced Functional Materials* 33, no. 15 (2023): 2211023.

38. B. Lu, H. Yuk, S. Lin, et al., "Pure PEDOT:PSS Hydrogels," *Nature Communications* 10, no. 1 (2019): 1043.

39. J. Liu, J. Garcia, L. M. Leahy, et al., "3D Printing of Multifunctional Conductive Polymer Composite Hydrogels," *Advanced Functional Materials* 33, no. 37 (2023): 2214196.

40. J. Rivnay, S. Inal, A. Salleo, R. M. Owens, M. Berggren, and G. G. Malliaras, "Organic Electrochemical Transistors," *Nature Reviews Materials* 3, no. 2 (2018): 1–14.

41. J. Rivnay, S. Inal, B. A. Collins, et al., "Structural Control of Mixed Ionic and Electronic Transport in Conducting Polymers," *Nature Communications* 7, no. 1 (2016): 11287.

42. Y. Xu, X. Yang, A. K. Thomas, et al., "Noncovalently Assembled Electroconductive Hydrogel," *ACS Applied Materials & Interfaces* 10, no. 17 (2018): 14418–14425.

43. S. Kim, H. Choi, D. Son, and M. Shin, "Conductive and Adhesive Granular Alginate Hydrogels for On-Tissue Writable Bioelectronics," *Gels* 9, no. 2 (2023): 167.

44. M. Suneetha, O. S. Moo, S. M. Choi, S. Zo, K. M. Rao, and S. S. Han, "Tissue-Adhesive, Stretchable, and Self-Healable Hydrogels Based on Carboxymethyl Cellulose-Dopamine/PEDOT:PSS via Mussel-Inspired Chemistry for Bioelectronic Applications," *Chemical Engineering Journal* 426 (2021): 130847.

45. A. R. Spencer, A. Primbetova, A. N. Koppes, R. A. Koppes, H. Fenniri, and N. Annabi, "Electroconductive Gelatin Methacryloyl-PEDOT:PSS Composite Hydrogels: Design, Synthesis, and Properties," *ACS Biomaterials Science & Engineering* 4, no. 5 (2018): 1558–1567.

46. A. R. Spencer, E. Shirzaei Sani, J. R. Soucy, et al., "Bioprinting of a Cell-Laden Conductive Hydrogel Composite," *ACS Applied Materials & Interfaces* 11, no. 34 (2019): 30518–30533.

47. D. N. Heo, S.-J. Lee, R. Timsina, X. Qiu, N. J. Castro, and L. G. Zhang, "Development of 3D Printable Conductive Hydrogel With Crystallized PEDOT:PSS for Neural Tissue Engineering," *Materials Science and Engineering: C* 99 (2019): 582–590.

48. F. Furlani, M. Montanari, N. Sangiorgi, et al., "Electroconductive and Injectable Hydrogels Based on Gelatin and PEDOT:PSS for a Minimally Invasive Approach in Nervous Tissue Regeneration," *Biomaterials Science* 10, no. 8 (2022): 2040–2053, https://doi.org/10.1039/D2BM00116K.

49. R. T. Hassarati, H. Marcal, L. John, R. Foster, and R. A. Green, "Biofunctionalization of Conductive Hydrogel Coatings to Support Olfactory Ensheathing Cells at Implantable Electrode Interfaces," *Journal of Biomedical Materials Research Part B: Applied Biomaterials* 104, no. 4 (2016): 712–722.

50. H. Zhang, J. Guo, Y. Wang, L. Sun, and Y. Zhao, "Stretchable and Conductive Composite Structural Color Hydrogel Films as Bionic Electronic Skins," *Advanced Science* 8, no. 20 (2021): 2102156.

51. Y. Cui, F. Zhang, G. Chen, et al., "A Stretchable and Transparent Electrode Based on PEGylated Silk Fibroin for In Vivo Dual-Modal Neural-Vascular Activity Probing," *Advanced Materials* 33, no. 34 (2021): 2100221.

52. T. Teshima, H. Nakashima, N. Kasai, et al., "Mobile Silk Fibroin Electrode for Manipulation and Electrical Stimulation of Adherent Cells," *Advanced Functional Materials* 26, no. 45 (2016): 8185–8193.

53. C. Gao, Y. Li, X. Liu, J. Huang, and Z. Zhang, "3D Bioprinted Conductive Spinal Cord Biomimetic Scaffolds for Promoting Neuronal Differentiation of Neural Stem Cells and Repairing of Spinal Cord Injury," *Chemical Engineering Journal* 451 (2023): 138788.

54. S. Song, X. Liu, J. Huang, and Z. Zhang, "Neural Stem Cell-Laden 3D Bioprinting of Polyphenol-Doped Electroconductive Hydrogel Scaffolds for Enhanced Neuronal Differentiation," *Biomaterials Advances* 133 (2022): 112639.

55. S. Song, Y. Li, J. Huang, S. Cheng, and Z. Zhang, "Inhibited Astrocytic Differentiation in Neural Stem Cell-Laden 3D Bioprinted Conductive Composite Hydrogel Scaffolds for Repair of Spinal Cord Injury," *Biomaterials Advances* 148 (2023): 213385.

56. V. R. Feig, S. Santhanam, K. W. McConnell, et al., "Conducting Polymer-Based Granular Hydrogels for Injectable 3D Cell Scaffolds," *Advanced Materials Technologies* 6, no. 6 (2021): 2100162.

57. B. K. Bhunia and B. B. Mandal, "Exploring Gelation and Physicochemical Behavior of In Situ Bioresponsive Silk Hydrogels for Disc Degeneration Therapy," *ACS Biomaterials Science & Engineering* 5, no. 2 (2018): 870–886.

58. A. Matsumoto, J. Chen, A. L. Collette, et al., "Mechanisms of Silk Fibroin Sol–Gel Transitions," *Journal of Physical Chemistry B* 110, no. 43 (2006): 21630–21638.

59. L. S. Wray, X. Hu, J. Gallego, et al., "Effect of Processing on Silk-Based Biomaterials: Reproducibility and Biocompatibility," *Journal of Biomedical Materials Research Part B: Applied Biomaterials* 99, no. 1 (2011): 89–101.

60. A. R. Murphy and D. L. Kaplan, "Biomedical Applications of Chemically-Modified Silk Fibroin," *Journal of Materials Chemistry* 19, no. 36 (2009): 6443–6450.

61. F. Agostinacchio, V. Fitzpatrick, S. Dire, D. L. Kaplan, and A. Motta, "Silk Fibroin-Based Inks for In Situ 3D Printing Using a Double Crosslinking Process," *Bioactive Materials* 35 (2024): 122–134.

62. M. Solazzo, K. Krukiewicz, A. Zhussupbekova, K. Fleischer, M. J. Biggs, and M. G. Monaghan, "PEDOT:PSS Interfaces Stabilised Using a PEGylated Crosslinker Yield Improved Conductivity and Biocompatibility," *Journal of Materials Chemistry B* 7, no. 31 (2019): 4811–4820.

63. M. Asplund, H. von Holst, and O. Inganäs, "Composite Biomolecule/PEDOT Materials for Neural Electrodes," *Biointerphases* 3, no. 3 (2008): 83–93.

64. M. Solazzo and M. G. Monaghan, "Hydrophilic, Conductive and Flexible Piezoresistive PEDOT:PSS 3D Sensors With Tunable Microarchitecture and Crosslinked Using a PEGylated Crosslinker," *Synthetic Metals* 290 (2022): 117157.

65. M. Solazzo and M. G. Monaghan, "Structural Crystallisation of Crosslinked 3D PEDOT:PSS Anisotropic Porous Biomaterials to Generate Highly Conductive Platforms for Tissue Engineering Applications," *Biomaterials Science* 9, no. 12 (2021): 4317–4328.

66. A. Carnicer-Lombarte, A. J. Boys, A. Güemes, et al., "Ultraconformable Cuff Implants for Long-Term Bidirectional Interfacing of Peripheral Nerves at Sub-Nerve Resolutions," *Nature Communications* 15, no. 1 (2024): 7523.

67. S. Zhang, P. Kumar, A. S. Nouas, L. Fontaine, H. Tang, and F. Cicoira, "Solvent-Induced Changes in PEDOT:PSS Films for Organic Electrochemical Transistors," *APL Materials* 3, no. 1 (2015): 014911.

68. A. Håkansson, S. Han, S. Wang, et al., "Effect of (3-Glycidyloxypropyl) Trimethoxysilane (GOPS) on the Electrical Properties of PEDOT: PSS

Films," *Journal of Polymer Science Part B: Polymer Physics* 55, no. 10 (2017): 814–820.

69. M. Thirumalaikumar, "Ring Opening Reactions of Epoxides. A Review," *Organic Preparations and Procedures International* 54, no. 1 (2022): 1–39.

70. E. Gutierrez-Fernandez, T. A. Ezquerra, and M.-C. García-Gutiérrez, "Additive Effect on the Structure of PEDOT:PSS Dispersions and Its Correlation With the Structure and Morphology of Thin Films," *Polymers* 14, no. 1 (2021): 141.

71. A. Soleimani-Gorgani, "Co-Solvents Roles in PEDOT:PSS Ink-Jet Inks," *Advances in Natural Sciences: Nanoscience and Nanotechnology* 9, no. 2 (2018): 025009.

72. P. Dubey, S. Kumar, S. Ravindranathan, et al., "pH Dependent Sophorolipid Assemblies and Their Influence on Gelation of Silk Fibroin Protein," *Materials Chemistry and Physics* 203 (2018): 9–16.

73. K. Roshanbinfar, L. Vogt, B. Greber, et al., "Electroconductive Biohybrid Hydrogel for Enhanced Maturation and Beating Properties of Engineered Cardiac Tissues," *Advanced Functional Materials* 28, no. 42 (2018): 1803951.

74. X. Wu, J. Hou, M. Li, J. Wang, D. L. Kaplan, and S. Lu, "Sodium Dodecyl Sulfate-Induced Rapid Gelation of Silk Fibroin," *Acta Biomaterialia* 8, no. 6 (2012): 2185–2192.

75. Q. Lu, X. Hu, X. Wang, et al., "Water-Insoluble Silk Films With Silk I Structure," *Acta Biomaterialia* 6, no. 4 (2010): 1380–1387.

76. P. Amorim, M. d'Ávila, R. Anand, P. Moldenaers, P. Van Puyvelde, and V. Bloemen, "Insights on Shear Rheology of Inks for Extrusion-Based 3D Bioprinting," *Bioprinting* 22 (2021): e00129.

77. S. R. Caliari and J. A. Burdick, "A Practical Guide to Hydrogels for Cell Culture," *Nature Methods* 13, no. 5 (2016): 405–414.

78. C. B. Pantazis, A. Yang, E. Lara, et al., "A Reference Human Induced Pluripotent Stem Cell Line for Large-Scale Collaborative Studies," *Cell Stem Cell* 29, no. 12 (2022): 1685–1702.

79. C. Liu, X. Du, S. Gao, et al., "A Cross-Linked Interconnecting Layer Enabling Reliable and Reproducible Solution-Processing of Organic Tandem Solar Cells," *Advanced Energy Materials* 10, no. 12 (2020): 1903800.

80. J. Jing, S. Liang, Y. Yan, X. Tian, and X. Li, "Fabrication of Hybrid Hydrogels From Silk Fibroin and Tannic Acid With Enhanced Gelation and Antibacterial Activities," *ACS Biomaterials Science & Engineering* 5, no. 9 (2019): 4601–4611.

81. P. Dubey, S. Kumar, V. K. Aswal, et al., "Silk Fibroin-Sophorolipid Gelation: Deciphering the Underlying Mechanism," *Biomacromolecules* 17, no. 10 (2016): 3318–3327.

82. P. Gupta, J. C. Moses, and B. B. Mandal, "Surface Patterning and Innate Physicochemical Attributes of Silk Films Concomitantly Govern Vascular Cell Dynamics," *ACS Biomaterials Science & Engineering* 5, no. 2 (2018): 933–949.

83. E. G. Langford, K. D. Shaughnessy, T. C. Devore, D. Lawrence, and C. Constantin, "Analysis of PEDOT:PSS Films After Sulfuric Acid Treatment on Silicon and Fused Silica Using FT-IR and UV-VIS," *MRS Advances* 1, no. 7 (2016): 465–469.

84. P. Sakunpongpitiporn, K. Phasuksom, N. Paradee, and A. Sirivat, "Facile Synthesis of Highly Conductive PEDOT:PSS via Surfactant Templates," *RSC Advances* 9, no. 11 (2019): 6363–6378.

85. N. D. Koromilas, G. C. Lainioti, E. K. Oikonomou, G. Bokias, and J. K. Kallitsis, "Synthesis and Self-Association in Dilute Aqueous Solution of Hydrophobically Modified Polycations and Polyampholytes Based on 4-Vinylbenzyl Chloride," *European Polymer Journal* 54 (2014): 39–51.

86. S. Sofia, M. B. McCarthy, G. Gronowicz, and D. L. Kaplan, "Functionalized Silk-Based Biomaterials for Bone Formation," *Journal of Biomedical Materials Research* 54, no. 1 (2001): 139–148.

87. A. Savva, J. Saez, A. Withers, et al., "3D Organic Bioelectronics for Electrical Monitoring of Human Adult Stem Cells," *Materials Horizons* 10, no. 9 (2023): 3589–3600.

88. G. Jiang, J. Sun, and F. Ding, "PEG-g-Chitosan Thermosensitive Hydrogel for Implant Drug Delivery: Cytotoxicity, In Vivo Degradation and Drug Release," *Journal of Biomaterials Science, Polymer Edition* 25, no. 3 (2014): 241–256.

89. C. Zhong, J. Wu, C. Reinhart-King, and C. Chu, "Synthesis, Characterization and Cytotoxicity of Photo-Crosslinked Maleic Chitosan–Polyethylene Glycol Diacrylate Hybrid Hydrogels," *Acta Biomaterialia* 6, no. 10 (2010): 3908–3918.

90. N. Johari, L. Moroni, and A. Samadikuchaksaraei, "Tuning the Conformation and Mechanical Properties of Silk Fibroin Hydrogels," *European Polymer Journal* 134 (2020): 109842.

91. Y. Cheng, L.-D. Koh, D. Li, B. Ji, M.-Y. Han, and Y.-W. Zhang, "On the Strength of β-Sheet Crystallites of *Bombyx mori* Silk Fibroin," *Journal of the Royal Society Interface* 11, no. 96 (2014): 20140305.

92. A. Karimi, A. Shojaei, and P. Tehrani, "Mechanical Properties of the Human Spinal Cord Under the Compressive Loading," *Journal of Chemical Neuroanatomy* 86 (2017): 15–18.

93. C. Fan, W. Yang, L. Zhang, et al., "Restoration of Spinal Cord Biophysical Microenvironment for Enhancing Tissue Repair by Injury-Responsive Smart Hydrogel," *Biomaterials* 288 (2022): 121689.

94. A. B. Kaiser, "Systematic Conductivity Behavior in Conducting Polymers: Effects of Heterogeneous Disorder," *Advanced Materials* 13, no. 12–13 (2001): 927–941.

95. R. Rubio-Govea, A. Opis-Basilio, A. Torres, M. Sánchez, K. Ray, and K. A. Mazzio, "Unveiling the Spectroscopic Signatures of Poly (3,4-Ethylenedioxythiophene) by Controlling Polaron and Bipolaron Concentrations," *Journal of Physical Chemistry C* 128 (2024): 18612–18621.

96. J. Li, Z. Li, J. Wang, and X. Chen, "Study of Conductive Polymer PEDOT:PSS for Infrared Thermal Detection," *Optical Materials Express* 9, no. 11 (2019): 4474–4482.

97. L. Peng and Z. Liu, "Enhancing Thermoelectric Properties by Using a Surface Polarization Effect Based on PEDOT:PSS Thin Films," *Journal of Materials Chemistry C* 7, no. 20 (2019): 6120–6128.

98. B. Gupta, M. Mehta, A. Melvin, et al., "Poly (3,4-Ethylenedioxythiophene) (PEDOT) and Poly (3,4-Ethylenedi oxythiophene)-Few Walled Carbon Nanotube (PEDOT-FWCNT) Nanocomposite Based Thin Films for Schottky Diode Application," *Materials Chemistry and Physics* 147, no. 3 (2014): 867–877.

99. R. Borah, G. C. Ingavle, A. Kumar, S. R. Sandeman, and S. V. Mikhalovsky, "Surface-Functionalized Conducting Nanofibers for Electrically Stimulated Neural Cell Function," *Biomacromolecules* 22, no. 2 (2021): 594–611.

100. M. A. Lampert and R. B. Schilling, "Current Injection in Solids: The Regional Approximation Method," in *Semiconductors and Semimetals*, vol. 6 (Amsterdam, Netherlands: Elsevier, 1970), 1–96.

101. B. Yang, C. Liang, D. Chen, et al., "A Conductive Supramolecular Hydrogel Creates Ideal Endogenous Niches to Promote Spinal Cord Injury Repair," *Bioactive Materials* 15 (2022): 103–119.

102. H. Teixeira, C. Dias, R. Veloso, A. Apolinário, and J. Ventura, "Tuning PEDOT:PSS Low-Impedance Thin Films With High Charge Injection for Microelectrodes Applications," *Progress in Organic Coatings* 168 (2022): 106894.

103. I. S. Romero, M. L. Schurr, J. V. Lally, M. Z. Kotlik, and A. R. Murphy, "Enhancing the Interface in Silk–Polypyrrole Composites Through Chemical Modification of Silk Fibroin," *ACS Applied Materials & Interfaces* 5, no. 3 (2013): 553–564.

104. T. Yucel, M. L. Lovett, and D. L. Kaplan, "Silk-Based Biomaterials for Sustained Drug Delivery," *Journal of Controlled Release* 190 (2014): 381–397.

105. A. Gangrade and B. B. Mandal, "Injectable Carbon Nanotube Impregnated Silk Based Multifunctional Hydrogel for Localized Targeted and On-Demand Anticancer Drug Delivery," *ACS Biomaterials Science & Engineering* 5, no. 5 (2019): 2365–2381.

106. Y. Guan, F. Sun, X. Zhang, et al., "Silk Fibroin Hydrogel Promote Burn Wound Healing Through Regulating TLN1 Expression and Affecting Cell Adhesion and Migration," *Journal of Materials Science: Materials in Medicine* 31, no. 5 (2020): 48, https://doi.org/10.1007/s10856-020-06384-8.

107. B. B. Mandal and S. C. Kundu, "Cell Proliferation and Migration in Silk Fibroin 3D Scaffolds," *Biomaterials* 30, no. 15 (2009): 2956–2965.

108. S. M. de Leeuw, S. Davaz, D. Wanner, et al., "Increased Maturation of iPSC-Derived Neurons in a Hydrogel-Based 3D Culture," *Journal of Neuroscience Methods* 360 (2021): 109254.

109. B. Rico, H. E. Beggs, D. Schahin-Reed, N. Kimes, A. Schmidt, and L. F. Reichardt, "Control of Axonal Branching and Synapse Formation by Focal Adhesion Kinase," *Nature Neuroscience* 7, no. 10 (2004): 1059–1069.

110. W. R. Kim, M. J. Jang, S. Joo, W. Sun, and Y. Nam, "Surface-Printed Microdot Array Chips for the Quantification of Axonal Collateral Branching of a Single Neuron In Vitro," *Lab on a Chip* 14, no. 4 (2014): 799–805.

111. D. Joung, V. Truong, C. C. Neitzke, et al., "3D Printed Stem-Cell Derived Neural Progenitors Generate Spinal Cord Scaffolds," *Advanced Functional Materials* 28, no. 39 (2018): 1801850.

112. T. Wang, G. Huang, Z. Yi, S. Dai, W. Zhuang, and S. Guo, "Advances in Extracellular Vesicle-Based Combination Therapies for Spinal Cord Injury," *Neural Regeneration Research* 19 (2023): 369–374.

113. H. Shen, C. Fan, Z. You, Z. Xiao, Y. Zhao, and J. Dai, "Advances in Biomaterial-Based Spinal Cord Injury Repair," *Advanced Functional Materials* 32, no. 13 (2022): 2110628.

114. X. Hu, W. Xu, Y. Ren, et al., "Spinal Cord Injury: Molecular Mechanisms and Therapeutic Interventions," *Signal Transduction and Targeted Therapy* 8, no. 1 (2023): 245.

Supporting Information

Additional supporting information can be found online in the Supporting Information section.